Geomorphology 268 (2016) 207–221

Contents lists available at ScienceDirect

Geomorphology

journal homepage: www.elsevier.com/locate/geomorph

Two early Holocene rock avalanches in the Bernese Alps (Rinderhorn, Switzerland)

Lorenz M. Grämiger [a,*], Jeffrey R. Moore [a,b], Christof Vockenhuber [c], Jordan Aaron [d], Irka Hajdas [c], Susan Ivy-Ochs [c,e]

[a] Department of Earth Sciences, ETH Zurich, Sonneggstrasse 5, 8092 Zurich, Switzerland
[b] University of Utah, Department of Geology and Geophysics, 115 South, 1460 East, Salt Lake City, UT, USA
[c] Laboratory of Ion Beam Physics, ETH Zurich, Otto-Stern-Weg 5, 8093 Zurich, Switzerland
[d] University of British Columbia, 6330 Stores Road, Vancouver, British Columbia V6T 1Z4, Canada
[e] Department of Geography, University of Zurich, Winterthurerstrasse 190, 8057 Zurich, Switzerland

ARTICLE INFO

Article history:
Received 23 January 2016
Received in revised form 1 June 2016
Accepted 7 June 2016
Available online 8 June 2016

Keywords:
Rock avalanche
Cosmogenic dating
Runout modeling
Seismic triggering

ABSTRACT

Large rock avalanches constitute a critical process modulating the evolution of alpine landscapes; however, the relatively infrequent occurrence of these high-magnitude events makes identifying underlying process controls challenging. Here we describe two rock avalanches in the Rinderhorn area of the Bernese Alps, Switzerland, providing new mapping of rock avalanche source areas and deposits, refined volume estimates for each event, runout modeling back-analyses, and absolute age constraint from cosmogenic ^{36}Cl surface exposure dating. Results reveal that the Daubensee rock avalanche released ~4 million m^3 of limestone sliding from the western crest of the Rinderhorn. Debris ran out across a Lateglacial moraine before reaching the valley bottom and spreading, leaving thin (on average 7 m) deposits across a broad area. The runout resulted in a Fahrböschung angle of 21°. Part of the deposit now lies beneath Lake Daubensee. The Klein Rinderhorn rock avalanche released ~37 million m^3 of limestone along a dip-slope sliding plane, with a maximum runout distance of 4.3 km and estimated Fahrböschung angle of 14°. Deposits bulked to ~47 million m^3 running up the opposing slope, with distinct hummocky morphology in the proximal area and a distal longitudinal flow ridge. These deposits were later modified and partly obscured by ice avalanches from the nearby Altels peak. Cosmogenic ^{36}Cl surface exposure dating revealed nearly coincident ages for both rock avalanches of 9.8 ± 0.5 ka. The large lag time between local deglaciation and failure suggests that the events were not directly triggered by deglaciation. Rather, the concurrent exposure ages, also coinciding with the nearby Kander valley rock avalanche as well as paleoseismic records from nearby lakes, strongly suggest seismic triggering.
© 2016 Elsevier B.V. All rights reserved.

1. Introduction

Deposits of large prehistoric rock avalanches are a common feature in many high alpine valleys (Heim, 1932; Abele, 1974), representing catastrophic bedrock failure and mass transport and, in many cases, exerting long-lasting control on the evolution of these landscapes (Korup, 2006). However, conclusions regarding the temporal occurrence and predominant drivers of these events remain elusive. Deglaciation is often proposed to be the primary cause of post-glacial alpine rock slope failures (Holm et al., 2004; Cossart et al., 2008). Ice is commonly assumed to act as a resisting force for oversteepened rock walls undercut by glacial erosion (Abele, 1974; Agliardi et al., 2009; Geertsema and Chiarle, 2013), which later collapse during deglaciation as they are left unsupported. However, a growing number of dated post-glacial landslides show lag times (i.e., time between deglaciation and slope failure) of thousands of years (e.g., Ivy-Ochs et al., 2009a; Prager et al., 2009; McColl, 2012; Ostermann et al., 2012; Ballantyne et al., 2014a, 2014b), contradicting this hypothesis. Moreover, the efficacy of glacial buttressing to provide significant lateral support to adjacent rock slopes has been called into question because of the ductile behavior of ice over long time scales (McColl et al., 2010; McColl and Davies, 2013). Therefore, debuttressing of valley slopes during glacial retreat is increasingly regarded as an unlikely predominant trigger for large paraglacial rock slope failures. Although glacier erosion may have acted as a preparatory factor by oversteepening rock walls during glaciation (Augustinus, 1995; Leith et al., 2014), other environmental processes following deglaciation reduce slope stability over time until catastrophic failure (Eberhardt et al., 2004; Prager et al., 2008; McColl, 2012). Holocene climate change toward warmer and wetter conditions is frequently proposed as a cause and

* Corresponding author.
E-mail address: graemiger.lorenz@gmail.com (L.M. Grämiger).

http://dx.doi.org/10.1016/j.geomorph.2016.06.008
0169-555X/© 2016 Elsevier B.V. All rights reserved.

trigger of large prehistoric landslides, which may affect temporal clustering (Prager et al., 2008; Ivy-Ochs et al., 2009a; Zerathe et al., 2014). Permafrost thaw, melting of snow and ice, frost weathering, and increased joint-water pressures caused by heavy rainfall are commonly invoked processes accompanying climate change (see discussion by McColl, 2012) but generally remain speculative for any given site.

Earthquake-induced rock slope failures are common in alpine regions (e.g., Jibson et al., 2006). Strong ground motion accompanying high magnitude (M > 6) earthquakes can trigger landslides over a variety of scales in spatially constrained areas (Keefer, 1984). In the Rhone valley of Switzerland, historical records dating back nearly 500 years describe several damaging earthquakes that each triggered at least one large landslide (Fritsche et al., 2012). Meanwhile, paleoseismic records from subaquatic mass movement stratigraphy in the Alps provide evidence for at least two episodes of increased neotectonic activity during the Lateglacial and late Holocene (Strasser et al., 2013), potentially coinciding with temporal clusters of subaerial landslides. Post-glacial isostatic rebound has been suggested to be the driver of these seismic episodes (Monecke et al., 2006; Strasser et al., 2013). Related studies in Scotland and Ireland exclude debuttressing as a direct trigger for the majority of dated rock slope failures, but further support stress release and uplift caused by glacial unloading as a predominant cause of landslide activity (Ballantyne et al., 2014a, 2014b). Periods of isostatically induced seismicity trail deglaciation, possibly explaining observed lag times of early Holocene landslide clusters (McColl, 2012).

Recent studies of prehistoric rock avalanches in the European Alps reveal intriguing spatiotemporal patterns, with several concurrent events during the late Pleistocene (e.g., Van Husen et al., 2007; Claude et al., 2014; Nagelisen et al., 2015). The first apparent temporal cluster of landslides appears during the early Holocene (~10–9 ka; Soldati et al., 2004; Prager et al., 2008), containing many of the largest known Alpine rockslides, e.g., Flims (Ivy-Ochs et al., 2009a) and Köfels (Ivy-Ochs et al., 1998; Nicolussi et al., 2015). A second peak of apparent increased landslide activity occurs during the Subboreal (5–3 ka; Soldati et al., 2004; Prager et al., 2008; Zerathe et al., 2014), including the large Fernpass event (Prager et al., 2009). As the total number of dated events in the Alps continues to grow, such temporal clusters may become more apparent, and new periods of enhanced landslide activity may be revealed. In addition, several spatial concentrations of slope failures have been observed in the Alps. Well-known spatial clusters occur, for example, around Flims/Chur in Switzerland (Abele, 1974; Ivy-Ochs et al., 2009a), the Fernpass region of Tyrol in Austria (Prager et al., 2008), and the Trentino Province in Italy (Abele, 1974; Soldati et al., 2004; Martin et al., 2014). In our study area in the Bernese Alps, Switzerland, between the Kander valley and Gemmi Pass, deposits of several large landslides are known, including the Kander valley rock avalanche (Tinner et al., 2005), the nearby Oeschinensee rock avalanche (Abele, 1974), as well as the Klein Rinderhorn and the Daubensee rock avalanches studied in detail here.

In this study, we investigate two large rock avalanches in the Rinderhorn region of the Bernese Alps: the Klein (Kl.) Rinderhorn rock avalanche and the Daubensee rock avalanche. We describe the release and deposit areas of each rock avalanche and present new cosmogenic nuclide surface exposure ages for the two events. Recreating pre-failure topography, we calculate source and deposit volumes and present runout models of both rock avalanches. The combined results enable better understanding of how changes in rock slope boundary conditions associated with glacier retreat, post-glacial seismicity, and Holocene climate change help to condition and trigger large rock slope failures and to provide new data for continued analysis of spatial and temporal clusters of large Alpine landslides.

2. Study area

Our study area (Fig. 1) is located between Kandersteg and Gemmi Pass in the Bernese Alps of Switzerland. The region features a high alpine valley trending NE-SW with its floor at an elevation of ~2000 m asl and mountains to the east rising above 3000 m asl. The release area of the Kl. Rinderhorn rock avalanche includes a large portion of the northern flank of the Kl. Rinderhorn (3003 m asl), while deposits cover the valley bottom from Schwarenbach to Sunnbüel (Fig. 1). The Daubensee rock avalanche originated from the western flank of the Rinderhorn (3448 m asl) and travelled north of Lake Daubensee. The two rock avalanche deposits are separated by <1 km.

Geology of the region is embedded in the Helvetic nappes, specifically the Doldenhorn nappe. The Kl. Rinderhorn rock avalanche deposit consists mainly of massive Valanginian limestone, which slid on top of the weaker shales and marly limestones of the Berriasian Formation along NW-dipping bedding (Furrer et al., 1956). The Daubensee rock avalanche is situated in the Jurassic Malm limestones (Tithonian limestone) (Furrer et al., 1956). Hydrology in the study area is controlled by karst features and affected by the rock avalanche deposits. Schwarenbach is the watershed divide; water originating from the Schwarz Glacier flows toward the Kander valley (Fig. 1). The two lakes, Daubensee and Schwarzenbachsee, have subsurface discharge toward the south. During high water levels at Lake Daubensee, surface drainage occurs through the rock avalanche debris, and temporary springs form at the northern end of the deposit (Furrer et al., 1956). Small lakes in the Arvenwald area contain water only during spring.

Fig. 1 displays glacier extents in our study area mapped from moraines and trimlines. The Last Glacial Maximum (LGM) in the Alps is dated at ~28 to 18 ka BP (Ivy-Ochs et al., 2008; Ivy-Ochs, 2015). High peaks in the region emerged from LGM ice slightly above 2000 m asl (Bini et al., 2009). After collapse of the LGM ice cap, the last Lateglacial readvance, termed the Egesen stadial, is coincident with the Younger Dryas at 12.8–11.5 ka BP (Alley et al., 1993). The main valley glacier at that time in our research area was the Lämmeren Glacier, which advanced north toward the Kander valley (Hantke, 1980). Ice from the Schwarz Glacier and the Altels Glacier joined the Lämmeren Glacier at Spittelmatte. The prominent Lateglacial moraine parallel to the Daubensee possibly relates to the Egesen stadial. With the onset of the Holocene, glaciers retreated but sustained a number of minor readvances, culminating in the Little Ice Age (LIA) around 1850 (Ivy-Ochs et al., 2009b). The latest time ice could have been present in the deposit area of the investigated rock avalanches was during the Egesen stadial, while the release areas were not in contact with valley glaciers since the end of the LGM.

3. Daubensee rock avalanche

The release area of the Daubensee rock avalanche (Fig. 2A, B) is located along the mountain crest west of the Rinderhorn summit in steep NW-dipping limestone. The source elevation varies between 2710 and 3070 m asl. At the highest point, the crest of the mountain ridge has collapsed. Scarps within the upper part of the release area reveal clear boundaries, while the lower boundary is uncertain. The structural setting in the release area is defined by three distinct fracture sets (Fig. 2B). Bedding planes (F1) dip ~30° NW. Joint set F2 strikes parallel to the bedding with a steep dip, while F3 strikes NW-SE, is steeply dipping, and follows fault structures. This predisposition enables planar sliding with step-path failure of tabular bodies. The basal sliding plane is mostly covered by debris today; only the upper part of the failure surface near the crest remains exposed. This surface follows bedding (F1) in the limestone. While the sliding plane is assumed to be continuous through the main part of the release area, in the upper portion it becomes stepped with intervening cliffs (F2).

Following the main flow path of the rock avalanche, the maximum runout distance is ~2.5 km (Fig. 1). Before reaching the deposit area, the rock avalanche passed several obstacles in transit, which resulted in some intermediate deposition. An accumulation of 10–20 m thick debris is found above a bedrock outcrop at 2430 m asl. Farther down the path of the rock avalanche at 2315 m asl, a Lateglacial moraine parallels the lake trending N–S (Fig. 2C). The moraine crest, and accompanying depression

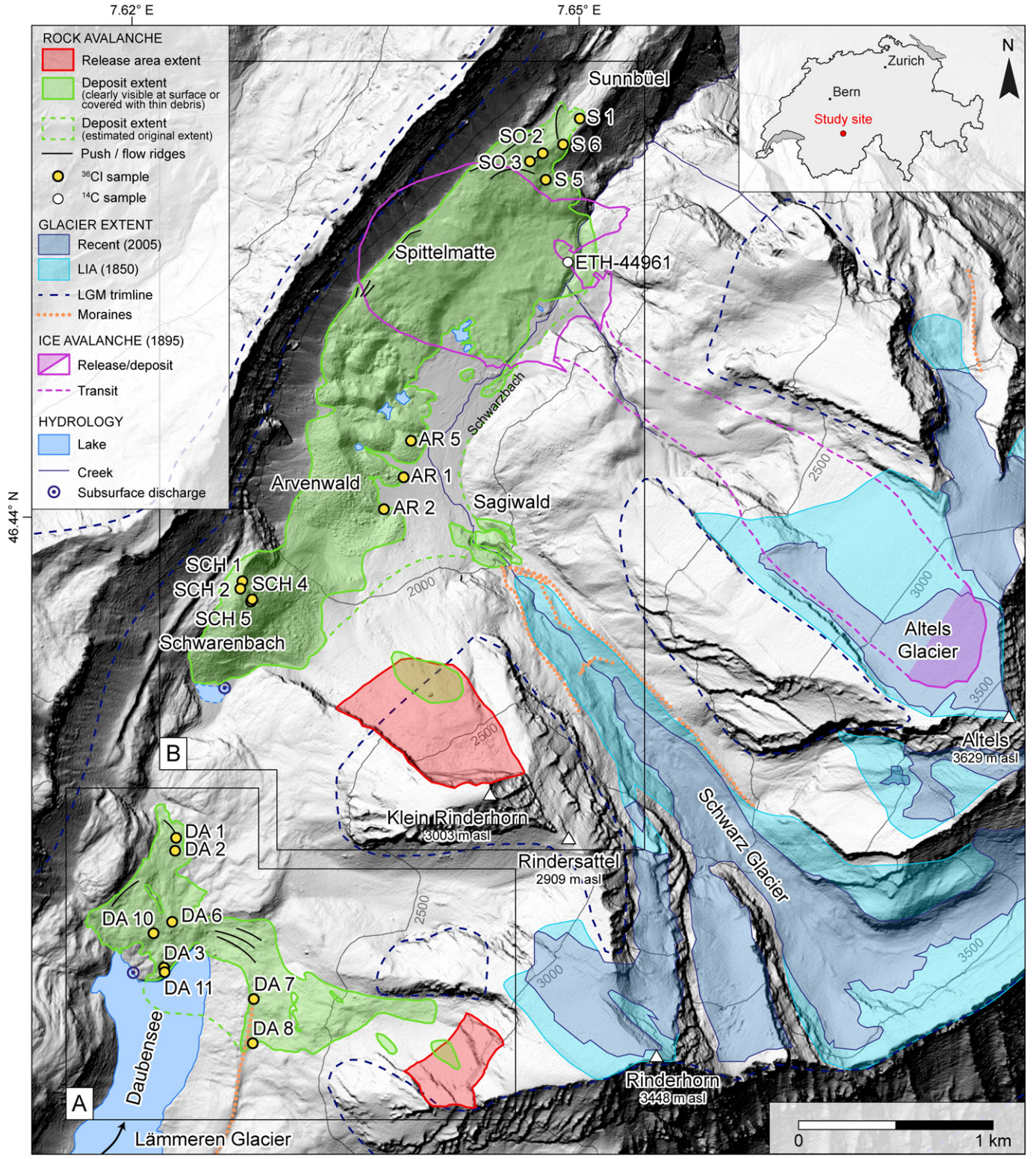

Fig. 1. Map of Rinderhorn rock avalanches. Inset showing study site in the Bernese Alps of Switzerland. Hillshade of digital elevation model (Swisstopo) for the Daubensee (A) and Kl. Rinderhorn (B) rock avalanches. Sample locations for ^{36}Cl and ^{14}C dating are marked. Lateglacial and Holocene glacier extents: recent (2005 orthoimage from Swisstopo), Little Ice Age (LIA) (Dufour Map from 1845–1865), and Last Glacial Maximum (LGM) (Bini et al., 2009). Features of the 1895 ice avalanche modified from Heim (1896).

on its uphill side, impounded rock avalanche debris over a distance of ~350 m. To the north, either the moraine has been breached by the rock avalanche or terminates naturally. Curved ridges along the flow path in this area appear as longitudinal flow bands, although their origin is uncertain (Fig. 1).

The main deposit at the head of Lake Daubensee (Fig. 2C) has a distinct and clear perimeter. Bedrock outcrops reveal a thin deposit of only a few meters depth. Large boulders are incorporated into the debris, and bedrock on the shore of Lake Daubensee is exposed in several places. Visible bedrock at the head of the lake shows a roche moutonnée-type

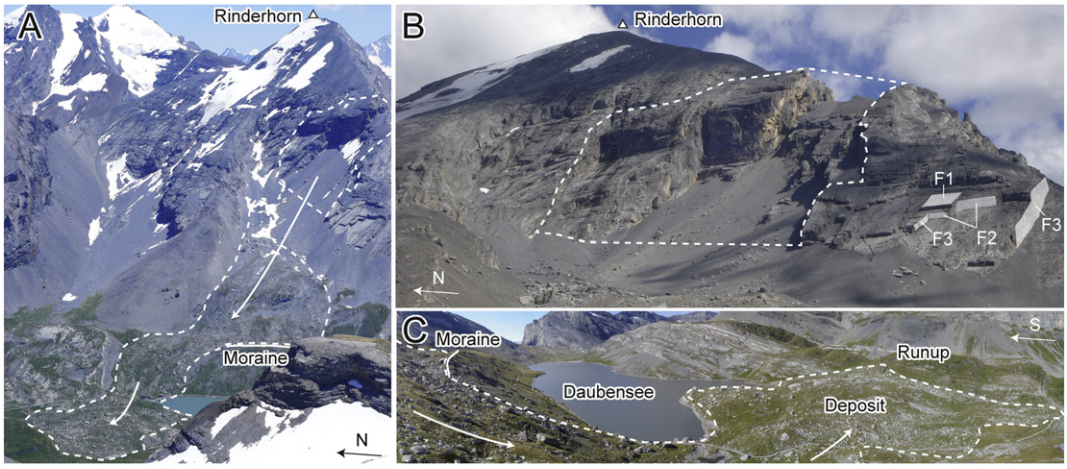

Fig. 2. Daubensee rock avalanche: (A) Overview showing release and deposit area (dashed line). Arrows indicate direction of rock avalanche motion. (B) Release area below the Rinderhorn summit (3448 m asl). Distinct fracture sets (F1, F2, F3) marked, defining structural setting of the release area. (C) Deposit north of Lake Daubensee and Lateglacial moraine.

landscape. To the west on the opposite side of the valley, the rock avalanche ran up to an elevation 2250 m asl. Runout was stopped at this point and trailing material surged, creating push-ridges striking N–S in the western part of the deposit. The distal (northern) end of the deposit lies at 2120 m asl, where the valley narrows. The Fahrböschung angle (relating fall height to travel distance along flow lines) for the Daubensee rock avalanche is 21°.

4. Klein Rinderhorn rock avalanche

4.1. Release and deposit area

The release area of the Kl. Rinderhorn rock avalanche (Fig. 3A) is located below the summit of the Kl. Rinderhorn (3003 m asl) in steep, NW-dipping limestone and is structurally predisposed by the same three fracture sets as the Daubensee slide (see Fig. 2B). The lateral extent of the Kl. Rinderhorn release area is defined by the head scarp (following F2) at 2960 m asl and a vertical cliff to the south (following F3). Clear indications of a lower boundary are not apparent from field evidence. The sliding plane follows NW-dipping bedding (F1) and is presently covered by debris. At Rindersattel (see location in Fig. 1), the continuation of the weak layer that acted as the sliding plane is visible in an outcrop, daylighting on the ridge; here strongly laminated marls are found interbedded with massive limestone (Fig. 3B).

The Kl. Rinderhorn deposit is displayed in Fig. 3 (see location in Fig. 1). The thick runup deposit at Schwarenbach reaches an elevation of 2183 m asl; blocky debris contains large angular limestone boulders and is sparsely vegetated. Large boulders are often surrounded by shattered rock pieces. The deposit at Arvenwald in the southern end of the valley has a strongly hummocky morphology (hills with heights between 10 and 50 m) and is covered with a pine forest. Small lakes with ephemeral water form in the depressions between hills. Alluvial deposits from the Schwarzbach fill most of the remaining low-lying area. The deposit at Sagiwald is located below LIA moraines of the Schwarz Glacier (Fig. 1); however, the extent of this deposit is unclear. Material mostly consists of angular cobbles with smaller boulders in a fine matrix, with a few large boulders incorporated. However, this deposit is clearly distinguishable from the adjacent LIA moraine, which is less weathered and not as blocky as the rock avalanche deposit. The LIA moraines terminate in the eroded deposit, meaning LIA glaciers did not reach farther than Sagiwald, which itself does not show any signs of Lateglacial modification. At Spittelmatte, the rock avalanche deposit exhibits a distinctly different morphology than at Arvenwald and Schwarenbach. Topography is gentle, without a hilly surface or forest cover. The deposit mainly consists of one large flow ridge striking N–S with thickness up to 60 m. We also observe smaller longitudinal flow ridges in this area. Only a few large boulders are apparent along the boundary with the Arvenwald and at the northern front of Spittelmatte. On the eastern side of the deposit, a steep erosional cutbank has been created by incision of a former course of the Schwarzbach creek. A fluvial terrace with small shallow ponds follows the recent alluvial plain at an elevation of 1880–1870 m asl, covering the rock avalanche deposit with a thin layer of debris; however, outcrops clearly show distinguishable rock avalanche deposits below. The distal limit of the rock avalanche is located at Sunnbüel, where lobes of debris are observed containing a few large boulders. The runout distance at this point is 4.3 km reaching an elevation of 1910 m asl, resulting in an estimated Fahrböschung angle for the rock avalanche of 14°.

A small gravel quarry on the east side of the Spittelmatte (see label ETH-44961 in Fig. 1) provides a geological section into the Kl. Rinderhorn deposit (Fig. 4). Underlying material consists of rock avalanche debris, evident as densely compacted, angular limestone components in a fine matrix with dark gray to bluish color. A silty clay layer with well-rounded cobbles rests on top of rock avalanche debris. The thickness of this layer varies; it is not continuous and dips slightly west. Several small fragments (1–20 mm) of charcoal were discovered within this layer, around 1 m below ground. The charcoal sample (ETH-44961) was prepared for dating following the protocol of Hajdas (2008). We obtained a radiocarbon age of 3660 ± 30 BP with accelerator mass spectrometry (AMS) using MICADAS (Wacker et al., 2010). The ^{14}C age was then converted to calendar ages with IntCal13 (Reimer et al., 2013) using the OxCal v4.2 program (Bronk Ramsey and Lee, 2013), resulting in a calendar age range of 4.085–3.899 cal ka BP (2σ). Above the clay, we distinguish at least three layers of debris by color that contain similar material. The matrix of these is sandy gravel with silt and clay, and they contain a large amount of subangular to rounded cobbles and boulders. Debris layers above the rock avalanche deposit thus provide evidence for subsequent erosional and depositional processes, post-slide fluvial modification of the Spittelmatte, as well as temporary ponded water bodies.

4.2. Altels ice avalanche

The steep, NW-dipping slope of the Altels, with its glaciated summit (3629 m asl), has a high predisposition for ice avalanches. Rock avalanche deposits of the Kl. Rinderhorn event are located in the transit and deposition area of these ice avalanches. Historical records exist for at least two ice avalanches: 18 August 1782 and 11 September 1895 (Heim, 1896; Faillettaz et al., 2011). The latter event was well documented by Heim (1896). In autumn 1895 the glacier below the Altels

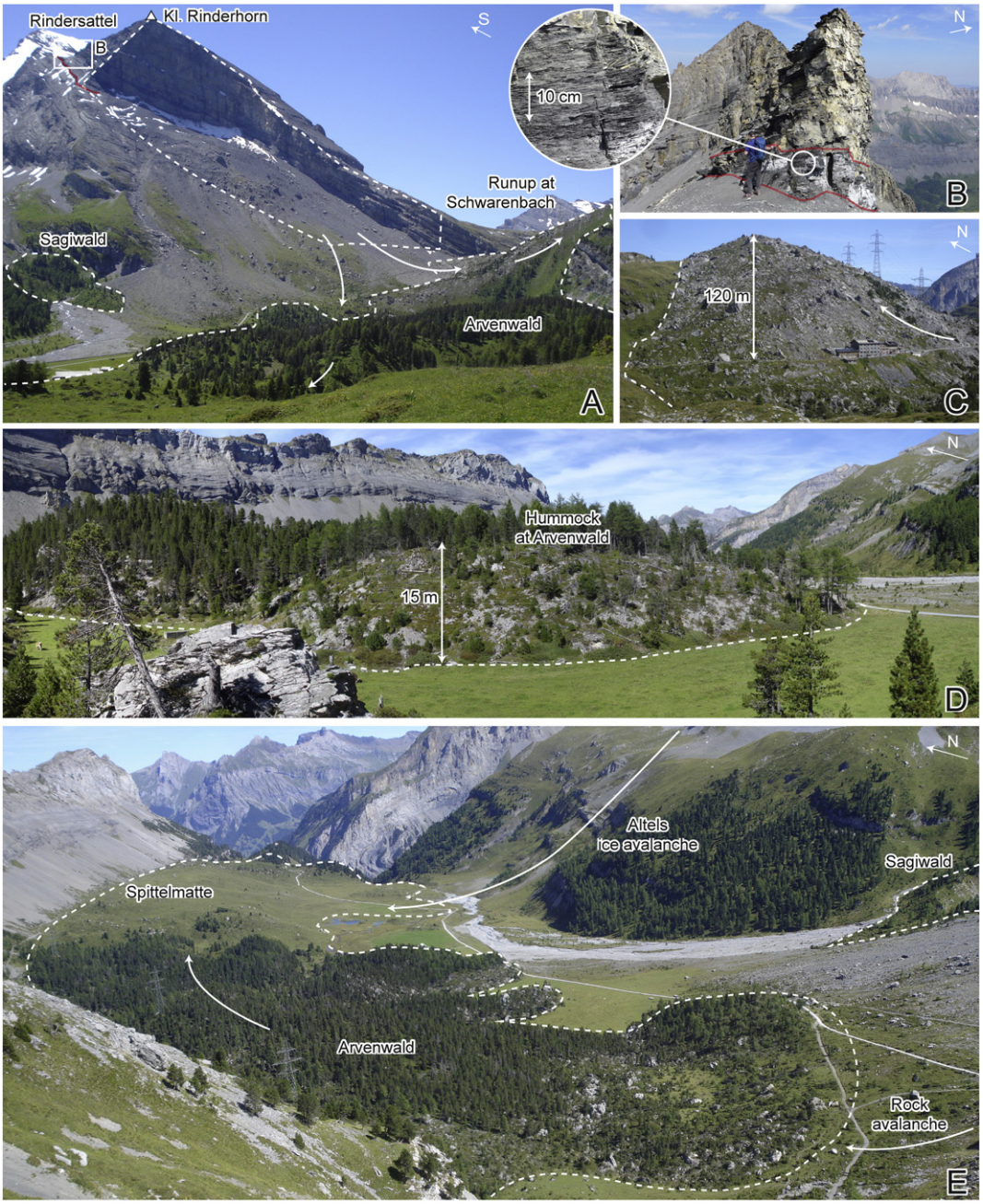

Fig. 3. Klein Rinderhorn rock avalanche: (A) Release and parts of the deposit area (dashed line) below the Kl. Rinderhorn summit (3003 m asl). Arrows indicate direction of rock avalanche motion. Weak layer (red line) that acted as the sliding plane daylighting at Rindersattel. (B) Outcrop of weak layer (red lines) composed of laminated marls (enlarged closeup) interbedded with limestones at Rindersattel. (C) Thick runup deposit at Schwarenbach. (D) Hummocky deposit and forest at Arvenwald. (E) Overview of the deposit at Arvenwald and Spittelmatte with the path of the 1895 Altels ice avalanche indicated.

summit failed in a catastrophic manner; about 4.5 million m^3 of ice broke free and slid to the valley below. The transit path ranges from below the summit of the Altels toward the valley at the Spittelmatte, where the main deposit came to rest (Figs. 1 and 3). The resulting air blast destroyed parts of the Arvenwald. Backflows of ice avalanche deposits were observed from the steep cut bank in the Spittelmatte, leaving behind almost undisturbed vegetation. On average, the cumulative percentage of emplaced rock debris was estimated by Heim (1896) to be about 1–2%, consisting of small, angular rock fragments. After melt of the ice avalanche deposit, the meadow of the Spittelmatte was covered with a layer of fine debris and small rocks; only in a few areas were larger boulders found. Observations from Heim (1896) thus demonstrate that the ice avalanche had mostly an aggradational effect at Spittelmatte, with almost no substrate erosion.

The 1782 ice avalanche was similar to the 1895 event but with a smaller impact area (Heim, 1896; Faillettaz et al., 2011). Only 113 years were thus necessary for the Altels Glacier to grow again and fail by 1895. We therefore assume that these (and similar) events were part of a potentially repeating process of periodic ice avalanches from the Altels. The Kl. Rinderhorn rock avalanche deposit is located within the transit and deposition area of these ice avalanches. Our field observations revealed a different, smoother surface of the rock avalanche deposit in the Spittelmatte region than in the adjacent Arvenwald. We suggest that periodic accumulation of debris by repeating Holocene ice avalanches might explain the difference in surface morphology (as well as vegetation). Further indication of the geomorphic effect of ice avalanches in the Spittelmatte area are large boulders (0.5–1 m^3) of siliceous limestone (Hauterivian) deposited in the middle

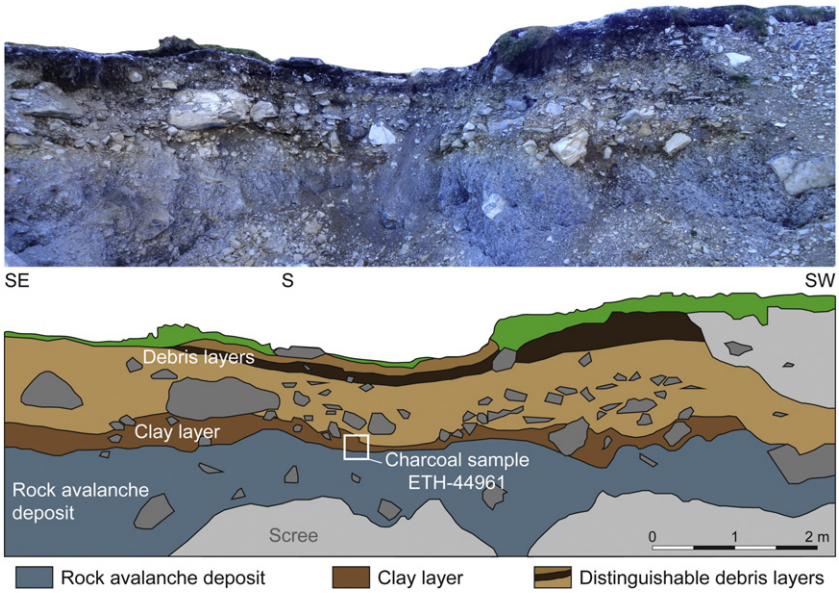

Fig. 4. Outcrop in the Spittelmatte (ETH-44961, Fig. 1) showing rock avalanche deposit covered by clay layer and distinguishable debris layers. Location of charcoal sample shown in clay layer used for radiocarbon dating, resulting in a calendar age range of 4.085–3.899 cal ka BP.

of the meadow. These are not part of the Kl. Rinderhorn source material and can only originate from the lower part of the Altels.

5. Cosmogenic nuclide surface exposure dating

Failure ages of the two Rinderhorn rock avalanches were investigated using cosmogenic nuclide surface exposure dating of deposited boulders. Following failure, fragmentation, and deposition of a rock avalanche, freshly created rock surfaces are exposed to bombardment from cosmic rays. Cosmogenic nuclides are produced gradually in exposed surfaces, which allows determining the absolute age of a rock avalanche (Ivy-Ochs and Kober, 2008). Cosmogenic ^{36}Cl exploited in this study for exposure dating of limestone is produced by several reactions: spallation of ^{40}Ca and ^{39}K, muon-induced reactions on ^{40}Ca and ^{39}K, and thermal and epithermal neutron capture by ^{35}Cl and ^{39}K (Gosse and Phillips, 2001).

We carefully selected boulders for sampling according to the criterion given by Ivy-Ochs and Kober (2008). We sampled 12 boulders from within the Kl. Rinderhorn deposit and 8 boulders from within the Daubensee deposit (Fig. 5). Sample locations are shown in Fig. 1. To obtain a more complete spatial description and to resolve uncertainties regarding failure scenarios, boulders from the three main parts of the Kl. Rinderhorn site were chosen, including the runup deposit at Schwarenbach, the hummocky deposit at Arvenwald, and the distal

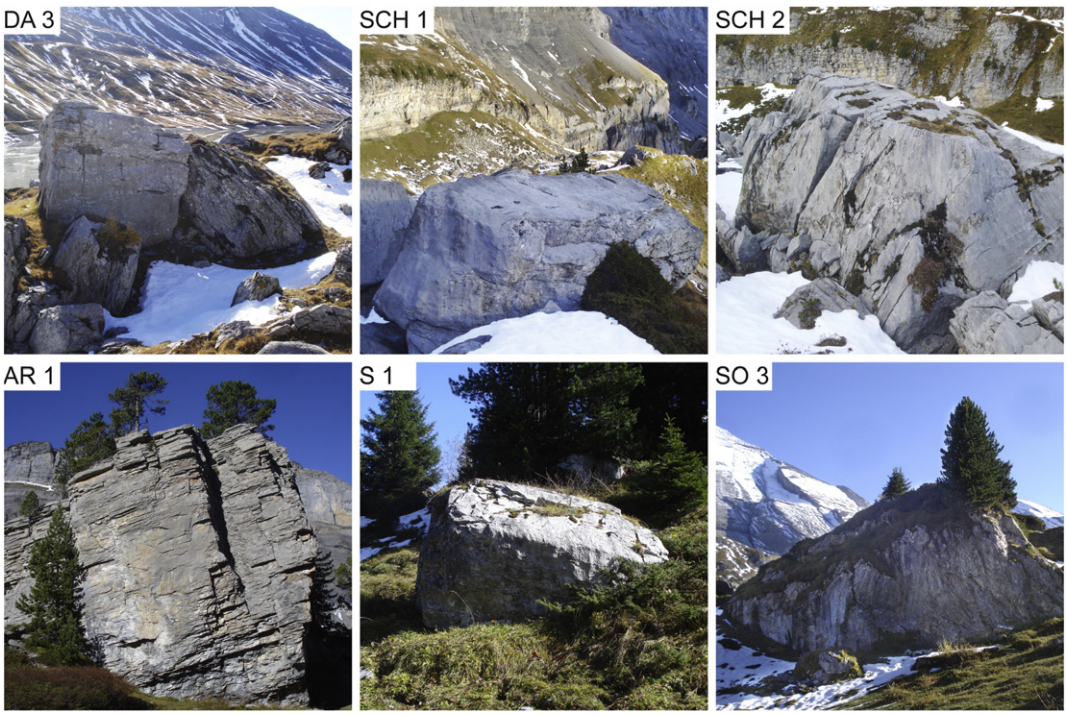

Fig. 5. Selected boulders chosen for surface exposure dating at the Daubensee and Kl. Rinderhorn deposits (see Table 1).

deposit at Sunnbüel. Boulders in the Spittelmatte area were avoided because of the unknown influence of the Altels ice avalanches.

Sample preparation and isotope dilution followed common procedures (Ivy-Ochs et al., 2004, 2009a). Total Cl and ^{36}Cl of the samples were measured with the 6 MV TANDEM at the AMS facility of the Laboratory of Ion Beam Physics, ETH Zurich (Table 1). The ETH internal standard K382/4 N with a value of $^{36}Cl/Cl = 17.36 \times 10^{-12}$ and the stable $^{37}Cl/^{35}Cl$ ratios to the natural ratio $^{37}Cl/^{35}Cl = 31.98\%$ were used to normalize the $^{36}Cl/^{35}Cl$ ratios of the samples (Christl et al., 2013). The ETH internal standard is calibrated against the primary ^{36}Cl standard KNSTD5000 (nominal ratio $(5.00 \pm 0.10) \times 10^{-12}$; Sharma et al., 1990). The measured sample ratios were corrected by subtracting full process chemistry blanks (3.4×10^{-15}). A production rate from Ca of 54.0 ± 3.5 atoms ^{36}Cl (g Ca)$^{-1}$ a^{-1} (Stone et al., 1996, 1998) was used to calculate surface exposure ages using a custom routine created by V. Alfimov based on the parameters described in Alfimov and Ivy-Ochs (2009). A density of 2.4 g cm^{-3} was assumed for all samples. Corrections for topographic shielding were calculated with the CRONUS-Earth online calculator (Balco et al., 2008). A typical surface erosion rate for karstified limestones of 0.5 cm ka^{-1} (Häuselmann, 2008) was assumed for all samples. No corrections for snow cover were applied. Major and minor element (B, Gd, Sm) concentrations (Table 2) were used to calculate the sample specific production rates following the procedures in Alfimov and Ivy-Ochs (2009).

Exposure ages from the Daubensee deposit range from 9.3 to 11.3 ka (Fig. 6). Excluding DA10, this scatter remains within the margins of error for each sample. The overall mean exposure age of the Daubensee rock avalanche is 10.0 ± 0.5 ka. The mean age excluding outlier DA10 is 9.8 ± 0.5 ka, which fits well with the peak age obtained using the "camel plot" approach (e.g., Balco, 2011), i.e., summing the Gaussian probability distributions of each measurement. Sample DA10 appears much older than the other dated boulders, which may indicate exposure prior to the rock avalanche.

Exposure ages for the Kl. Rinderhorn deposit are more scattered, ranging from 7.6 to 11.6 ka (Fig. 6). The mean exposure age for all samples is 9.7 ± 0.5 ka. Excluding four outliers (SCH2, S1, SO2, SO3), the mean age is 9.8 ± 0.5 ka, which matches the peak age obtained from the "camel plot". SCH2 and SO3 show markedly younger ages, likely because of post-depositional shielding, spalling of the boulder surface, or karst erosion (Ivy-Ochs and Kober, 2008). Ages of S1 (11.6 ± 0.7 ka) and SO2 (11.2 ± 0.6 ka) are close to the Younger Dryas (YD) and may be explained by entrainment of possible Egesen moraines. The choice of boulders at Sunnbüel was limited, and the selected sites were often covered by vegetation (e.g., SO2, SO3, S5; Fig. 5). Such suboptimal sampling conditions, in contrast to the more favorable Schwarenbach and Arvenwald sites, may have led to larger scatter in the resulting exposure ages. The exposure ages at Sunnbüel are not fully convincing as to the continuity of the deposit, but outcrops (e.g., Fig. 4) confirm the presence of rock avalanche material in this distal region.

Our dating results suggest that the Daubensee and Kl. Rinderhorn rock avalanches were coeval at 9.8 ± 0.5 ka, and alternative approaches for interpreting the exposure ages (i.e., "camel plots") yielded similar results. The two rock avalanches thus occurred roughly 1.7 ka after the end of the YD. During the YD, glacial ice of the Egesen stadial likely occupied the deposit areas of our study site for the final time, while the release areas of both rock avalanches were last in contact with valley glaciers during the LGM. The spatial distribution of ages supports the hypothesis that each rock avalanche occurred as a single, catastrophic event. Furthermore, the relatively large lag time after the LGM and YD rules out the possibility that the transit path was covered by ice. The radiocarbon age of the charcoal sample (ETH-44961) provides a minimum age and is not in conflict with exposure ages for the Kl. Rinderhorn event. Because the deposit at Sagiwald in front of LIA moraines of the Schwarz Glacier (Figs. 1 and 3) does not show evidence of glacial modification, we assume that by the time of failure (9.8 ka), the Schwarz Glacier had already retreated behind this extent (see also Ivy-Ochs et al., 2009b). The presence of hummocks and thick deposits in the proximal Arvenwald region supports the absence of ice within the deposit area (Robinson et al., 2014).

6. Reconstruction of pre-failure topography and volume analysis

Reconstruction of pre-failure topography is necessary for volume calculation and runout modeling. We recreated pre-failure topography by modifying the modern topography (swissALTI3D 2013 DEM by

Table 1
AMS measured concentrations of ^{36}Cl and calculated surface exposure ages.

Sample name	Latitude (DD.DDD)	Longitude (DD.DDD)	Elevation (m asl)	Site setting	Thickness (cm)	Shielding corr. factor	Cl (ppm)	Cl error (%)	^{36}Cl conc. (at g^{-1} × 10^6)	^{36}Cl conc. error (%)	Exposure age (ka)
Daubensee											
DA 1	46.424	7.622	2173	Front deposit	1.5	0.978	4.1	0.3	0.979	3.3	9.27 ± 0.43
DA 2	46.423	7.622	2178	Front deposit	1.0	0.978	9.2	0.3	1.090	4.4	10.03 ± 0.55
DA 3	46.418	7.621	2227	Main deposit	1.0	0.985	7.5	1.5	1.173	3.7	10.38 ± 0.51
DA 6	46.420	7.622	2230	Main deposit	1.5	0.985	5.1	1.1	1.154	2.5	10.11 ± 0.42
DA 7	46.416	7.627	2311	Behind moraine	2.0	0.980	6.1	1.3	1.045	3.2	9.38 ± 0.43
DA 8	46.414	7.627	2315	Behind moraine	1.5	0.976	7.2	2.5	1.162	4.2	9.61 ± 0.52
DA 10	46.419	7.620	2243	Main deposit	2.5	0.985	8.0	0.3	1.300	2.2	11.29 ± 0.45
DA 11	46.418	7.621	2223	Main deposit	3.5	0.981	6.6	1.2	1.115	5.3	9.96 ± 0.62
Kl. Rinderhorn											
SCH 1	46.436	7.626	2174	Schwarenbach	1.5	0.977	10.1	0.6	1.037	4.7	9.69 ± 0.56
SCH 2	46.435	7.626	2178	Schwarenbach	1.0	0.978	8.9	1.0	0.831	3.8	7.55 ± 0.38
SCH 4	46.435	7.627	2160	Schwarenbach	1.0	0.982	16.6	0.7	1.039	5.3	9.61 ± 0.60
SCH 5	46.435	7.627	2162	Schwarenbach	1.5	0.980	5.7	0.4	0.948	3.9	8.81 ± 0.45
AR 1	46.441	7.637	1902	Arvenwald	1.0	0.973	8.1	1.3	0.805	5.1	9.65 ± 0.58
AR 2	46.439	7.636	1899	Arvenwald	0.75	0.963	5.8	0.5	0.816	3.8	9.69 ± 0.49
AR 5	46.442	7.638	1910	Arvenwald	2.0	0.974	7.4	1.5	0.847	3.7	9.77 ± 0.48
S 1	46.457	7.649	1933	Sunnbüel	1.5	0.961	16.5	1.2	1.096	4.9	11.63 ± 0.68
SO 2	46.456	7.647	1927	Sunnbüel	1.5	0.962	21.8	1.0	1.046	3.9	11.22 ± 0.58
SO 3	46.455	7.646	1932	Sunnbüel	2.0	0.958	11.7	1.1	0.688	4.7	7.78 ± 0.45
S 5	46.454	7.647	1914	Sunnbüel	1.5	0.963	5.6	0.1	0.916	2.6	10.30 ± 0.43
S 6	46.456	7.648	1935	Sunnbüel	2.0	0.962	19.5	0.6	0.999	3.1	10.53 ± 0.48

Table 2
Major and minor element concentrations for the analyzed samples determined by XRF at XRAL, Ontario, Canada; samples denoted with (*) were determined by XRF at ETH Zurich (n.d. = not determined).

Sample name	Al_2O_3 (wt%)	CaO (wt%)	Cr_2O_3 (wt%)	Fe_2O_3 (wt%)	K_2O (wt%)	MgO (wt%)	MnO (wt%)	Na_2O (wt%)	P_2O_5 (wt%)	SiO_2 (wt%)	TiO_2 (wt%)	Total (wt%)	B (ppm)	Gd (ppm)	Sm (ppm)	Th (ppm)	U (ppm)
DA 1	0.52	53.20	<0.01	0.19	0.08	0.34	<0.01	<0.1	0.01	2.73	0.02	57.09	<10	0.29	0.20	0.10	0.64
DA 2	0.29	53.90	<0.01	0.12	0.04	0.43	<0.01	<0.1	0.01	1.43	0.02	56.24	<10	0.29	0.20	<0.1	0.53
DA 3	0.37	54.30	<0.01	0.16	0.04	0.47	<0.01	<0.1	0.02	2.18	0.01	57.55	<10	0.24	0.30	0.30	0.87
DA 6*	0.14	55.13	0.00	0.06	0.02	0.67	0.01	0.00	0.03	0.36	0.01	56.42	n.d.	n.d.	n.d.	0.00	0.00
DA 7	0.36	51.00	<0.01	0.14	0.05	0.57	<0.01	<0.1	0.02	2.21	0.02	54.37	<10	0.39	0.20	<0.1	0.88
DA 8*	0.13	55.22	0.00	0.08	0.02	0.56	0.01	0.00	0.02	0.39	0.01	56.44	n.d.	n.d.	n.d.	0.00	0.00
DA 10*	0.17	55.21	0.00	0.08	0.02	0.69	0.01	0.00	0.03	0.38	0.01	56.58	n.d.	n.d.	n.d.	0.00	0.00
DA 11*	0.17	55.13	0.00	0.07	0.02	0.71	0.01	0.00	0.03	0.42	0.01	56.57	n.d.	n.d.	n.d.	0.00	0.00
SCH 1	0.34	53.20	<0.01	0.21	0.05	0.91	<0.01	<0.1	<0.01	1.54	0.02	56.27	<10	0.23	0.20	<0.1	1.06
SCH 2	0.31	54.20	<0.01	0.18	0.04	0.60	<0.01	<0.1	<0.01	1.41	0.02	56.76	<10	0.18	0.20	<0.1	1.06
SCH 4*	0.64	52.44	0.00	0.30	0.07	2.03	0.01	0.00	0.01	1.49	0.03	57.02	n.d.	n.d.	n.d.	0.00	0.00
SCH 5	0.27	54.50	<0.01	0.23	0.03	0.41	<0.01	<0.1	<0.01	1.43	0.02	56.89	<10	0.25	0.20	<0.1	0.76
AR 1	0.90	50.30	<0.01	0.66	0.13	0.52	0.02	0.20	0.01	6.02	0.04	58.80	<10	0.79	0.80	1.10	0.51
AR 2	0.73	51.60	<0.01	0.33	0.10	0.46	<0.01	0.10	<0.01	5.35	0.04	58.71	<10	0.37	0.30	0.30	2.06
AR 5	0.44	52.70	<0.01	0.27	0.06	0.54	<0.01	<0.1	<0.01	2.41	0.03	56.45	<10	0.34	0.30	0.20	0.79
S 1*	0.13	55.47	0.00	0.05	0.02	0.67	0.01	0.00	0.04	0.23	0.01	56.62	n.d.	n.d.	n.d.	0.00	0.00
SO 2	0.22	53.80	<0.01	0.18	0.03	0.53	<0.01	<0.1	0.03	1.24	0.01	56.04	<10	0.27	0.20	<0.1	0.40
SO 3	0.42	52.60	<0.01	0.20	0.07	0.65	<0.01	<0.1	0.02	2.82	0.03	56.81	<10	0.52	0.50	0.10	0.65
S 5*	0.11	54.74	0.00	0.05	0.02	1.02	0.00	0.00	0.03	0.39	0.01	56.36	n.d.	n.d.	n.d.	0.00	0.00
S 6*	0.10	55.27	0.00	0.06	0.01	0.59	0.01	0.00	0.03	0.19	0.01	56.26	n.d.	n.d.	n.d.	0.00	0.00

Swisstopo) in the release, transit, and deposit areas of both rock avalanches, based on field and remote thickness estimates. Topographic contour lines from modern topography were modified and DEM data interpolated to reconstruct the pre-failure surface. The recreated topography was then adjusted as necessary to provide a smooth transition with surrounding terrain. We subtracted the reconstructed pre-failure topography from the modern topography (DEM) to calculate a height difference map. Volumes were determined by integrating over the area of the thickness raster. Total volumes in the deposit and release areas for each event were adjusted in an iterative process so that the released volumes matched the deposit volumes accounting for a typical fragmentation bulking factor of about 25% (Hungr and Evans, 2004). Post-slide deposit erosion was not taken into account in our volume analysis, and material entrainment during emplacement was neglected (not supported by field evidence).

Fig. 7 compares hillshade images of the post- and pre-failure topography at the Daubensee site. The release area was reconstructed by extrapolating adjacent topographic surfaces assuming similar inclination. Deposited rock avalanche debris was removed from the transit area. Accumulated debris behind the moraine was also removed to form a depression of similar size as in the adjacent unaffected area. The moraine was not extended to the north as the breaching processes cannot be

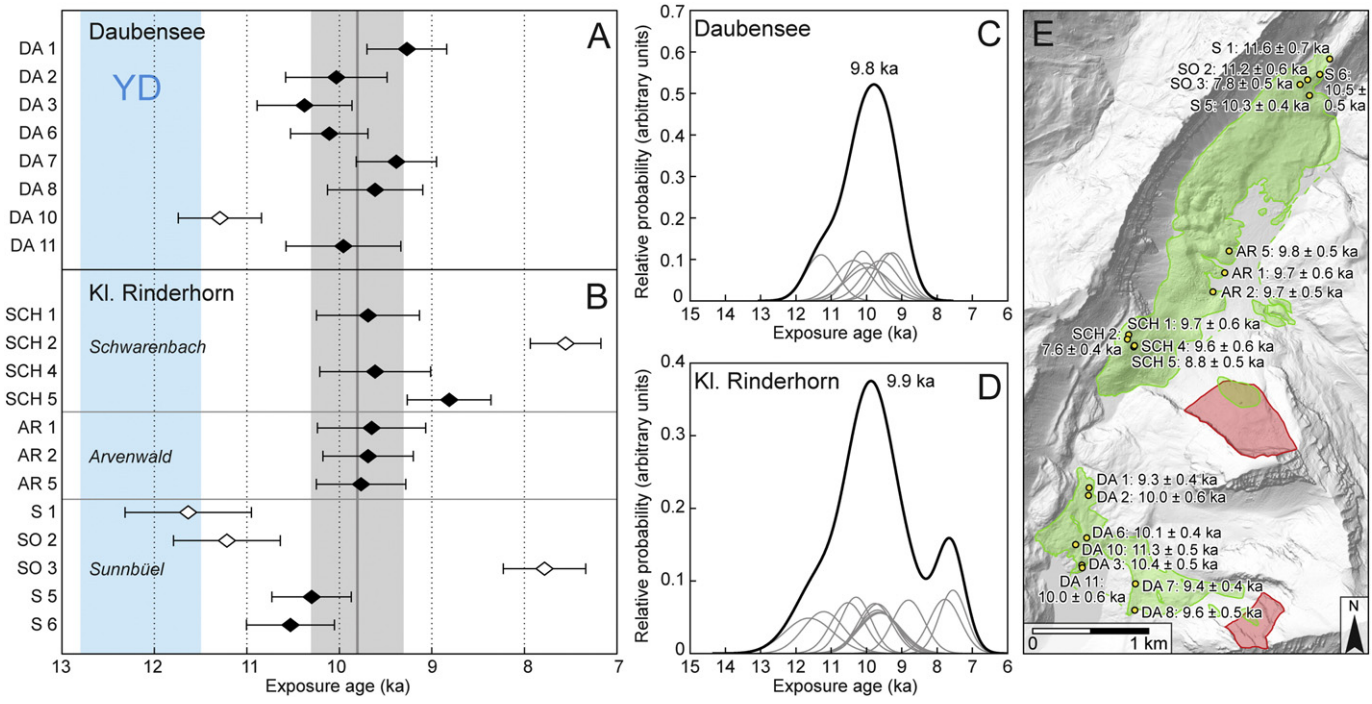

Fig. 6. Exposure ages of the Rinderhorn rock avalanches: (A) and (B) show exposure ages with error bars. Excluding outliers (shown as open symbols), the mean age of 9.8 ± 0.5 ka for the individual events is indicated by the gray bar. Younger Dryas (YD) period is indicated in blue shading (12.8–11.5 ka BP). (C) and (D) show "camel plots" of all ages with peak ages of 9.8 and 9.9 ka for the Daubensee and Kl. Rinderhorn rock avalanches, respectively. (E) Locations of sampled boulders (yellow) with calculated exposure ages, deposit extents (green), and release area extents (red).

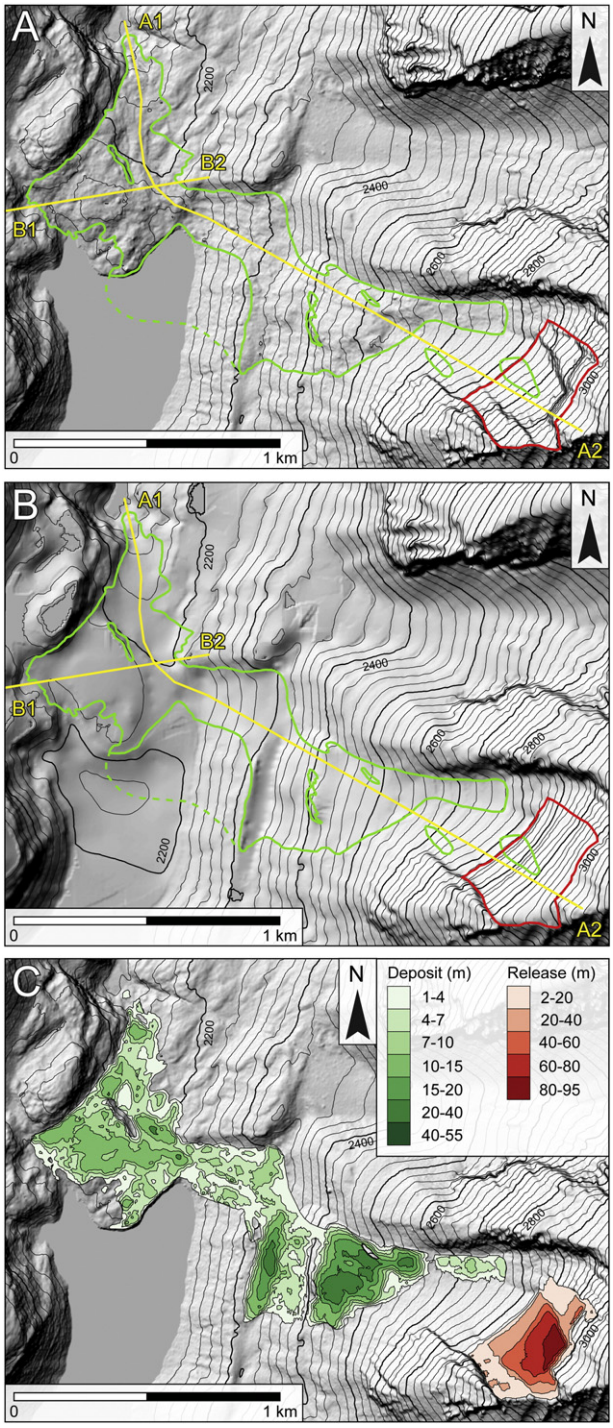

Fig. 7. Volume analysis for the Daubensee rock avalanche: (A) Post-failure surface (DTM by Swisstopo), (B) estimated pre-failure surface, and (C) calculated height difference. Contour interval is 20 m. Longitudinal profile along runout path and cross section through deposit (yellow lines) displayed in Fig. 10. Mapped release area (red line) and deposit area (green line) are shown.

recreated in subsequent runout modeling. The pre-failure surface in the main deposit area was reconstructed with the aid of bedrock outcrops and field estimations of deposit thickness. Because the amount of deposit in Lake Daubensee is unknown, calibrating the release volume until it matched the deposit volume with a reasonable bulking factor was not possible. Instead, the release volume was adjusted until the volume of the onshore deposit in the runout models (assuming a bulking factor of 25%) matched the calculated onshore volume from the field.

We compare reconstructed pre-failure topography to modern topography at the Kl. Rinderhorn site in Fig. 8. The steep cliff at the crest of the release area was reconstructed assuming similar dip as the neighboring slopes in order to obtain the released volume. Mapped deposits were subtracted from the current topography. The Spittelmatte area was modeled as a relatively flat alluvial plain dipping gently toward the outflow point of the Schwarzbach creek. Similar geomorphology is observed higher in the valley today. The topography at Schwarenbach was recreated as a steep bedrock ridge, as indicated in exposed surfaces adjacent to the deposit.

The release and deposit volumes for each rock avalanche were calculated by subtracting the pre-failure topography from the post-failure (present) topography; resulting height differences (i.e., deposit thicknesses) are displayed in Figs. 7 and 8. Cumulative volumes are listed in Table 3 for both events. The estimated onshore deposit volume of 4.2 million m^3 for the Daubensee rock avalanche is distributed thinly at the end of Lake Daubensee. Thick deposits of >20 m accumulated behind the Lateglacial moraine and in the transit area. The average thickness is around 7 m. The released volume of the Daubensee rock avalanche was estimated to be 4.4 million m^3, and we assume that a significant additional volume is deposited in the present-day Lake Daubensee (also verified by runout models). The Kl. Rinderhorn rock avalanche is an order of magnitude larger, with estimated deposit volume of 46.6 million m^3. The main body of the deposit lies at Schwarenbach with maximum thickness of 135 m. The hummocky topography at Arvenwald and Spittelmatte consists of hills up to 60 m high. The overall deposit has an average thickness of 22 m. The estimated released volume of 36.7 million m^3 results in a fragmentation bulking factor of 27%. Observed Fahrböschung angles for both events are typical for rock avalanches of similar volumes, matching well with empirical data relating volume and runout (Hungr et al., 2005, and references therein). Other recently investigated carbonate rock avalanches with comparable volumes also had similar Fahrböschung angles (e.g., Patzelt, 2012; Nagelisen et al., 2015).

7. Runout analysis

Numerical runout simulation was performed for the Daubensee and Kl. Rinderhorn rock avalanches using the code DAN3D (Hungr, 1995; McDougall and Hungr, 2004). The program models flow of an "equivalent fluid" over user-input three-dimensional terrain (Hungr and McDougall, 2009). We used a modified version of DAN3D that simulates the initially coherent landslide body transitioning into a flow-like rock avalanche by treating the initial sliding mass as a flexible block (Aaron and Hungr, 2016). The aim of our modeling was to simulate rock avalanche runout, predict deposit extents and thickness to compare with field estimates, and to verify the hypothesized single-event failure scenarios. Reconstructed pre-failure topography served as the path topography, and estimated thickness in the release area provided the source volume. For both rock avalanches, we assumed frictional basal rheology with an initial coherent sliding phase of 10 s. Rheology parameters (basal friction angle φ_b, internal friction angle φ_i, and pore pressure coefficient r_u) were adjusted by trial-and-error to match the total runout distance and lateral spreading of the deposit (Sosio et al., 2011). Note that φ_b represents the basal flow resistance of the rock avalanche, while φ_i affects the material spreading. Erosion and entrainment were neglected. Pore pressure coefficients were held at zero and unit weights set to 24 kN m^{-3}. Bulking during initial fragmentation cannot be simulated in DAN3D, therefore the release volume was increased by the previously determined bulking factors (Table 3). All terrain data and simulation outputs had spatial grid resolution of 5 m.

Optimal runout results for the Daubensee rock avalanche were achieved assuming a basal friction angle of 22° and an internal friction angle of 25°. Fig. 9 displays the modeled runout at different times, as well as the final simulated deposit after 70 s. The modeled runout reached a maximum velocity of ~95 m s^{-1}. Cross sections through the

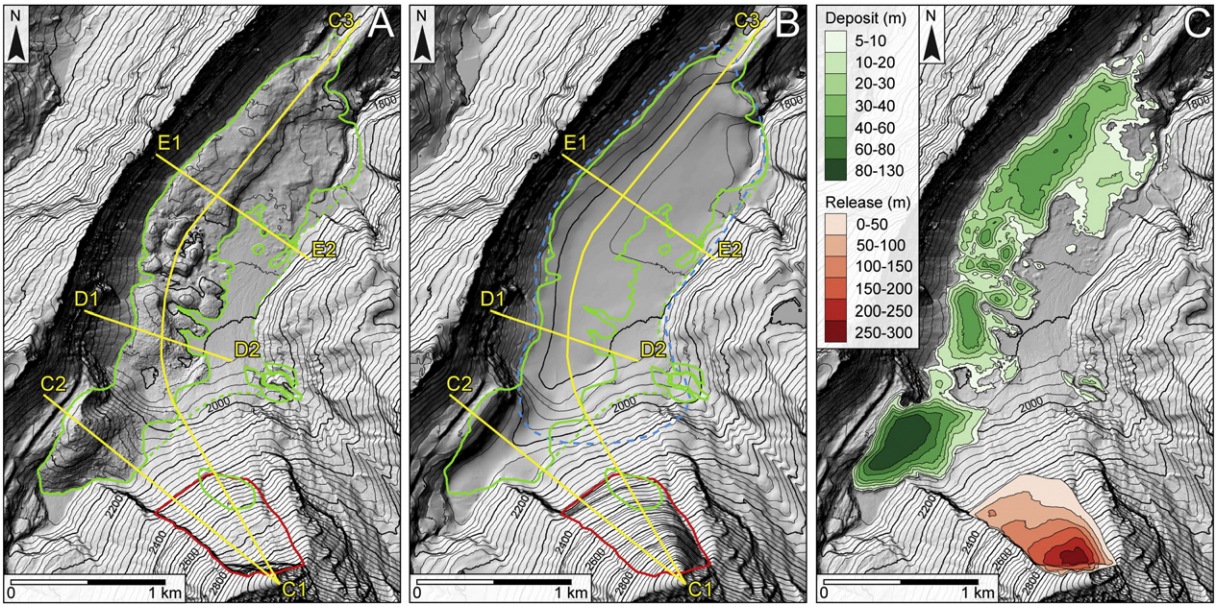

Fig. 8. Volume analysis for the Kl. Rinderhorn rock avalanche: (A) post-failure surface (DTM by Swisstopo), (B) estimated pre-failure surface, and (C) calculated height difference. Contour interval is 20 m. Longitudinal profile along runout path and cross sections through deposit (yellow lines) displayed in Fig. 12. Mapped release area (red line) and deposit area (green line) are shown. Light-blue dashed line delineates the valley sediments assigned lower friction angle in our runout model.

runout path comparing pre-failure topography, post-failure topography, and modeled deposit are shown in Fig. 10. Modeled deposit extents match mapped extents well in the northern and western areas. Modeled thicknesses are within the same range as field estimates, although lateral spreading at the head of Lake Daubensee does not resemble field observations. The stranded deposit high in the transit area was adequately reproduced. The mapped runout at Daubensee, including deposits interacting with the Lateglacial moraine and within Lake Daubensee, was challenging to recreate. Material retention behind the moraine was not adequately achieved in our models, and runout behavior was strongly controlled by the recreated depression at Lake Daubensee. We note that the topography of the lake bottom was estimated as no bathymetry data are currently available. Assuming 25% bulking, we estimate a source volume of 5.5 million m^3. Runout models resulted in an onshore deposit volume of 4.0 million m^3, with 1.5 million m^3 in the lake. The onshore volume agrees well with our field estimate of 4.2 million m^3.

The main challenge in modeling the Kl. Rinderhorn rock avalanche was simultaneous generation of a long runout toward the northern distal end of the deposit and limited proximal runup at Schwarenbach. Optimal results were achieved assuming a basal friction angle of 22° and an internal friction angle of 25°, with a reduced friction angle of 12° in the valley sediments of the alluvial plain (light-blue dashed line in Fig. 8). The modeled deposit at several time intervals is presented in Fig. 11 along with the final simulated deposit after 90 s. Fig. 12 compares pre- and post-failure topography with model results along longitudinal cross sections. Overall our simulation captured the general runout behavior of the Kl. Rinderhorn rock avalanche in a satisfactory manner. Runup at Schwarenbach was reproduced, although the field-estimated thickness is greater than the modeled deposit. The total runout distance at Spittelmatte and Sunnbüel is underestimated, and simulated deposits have more evenly distributed thickness than observed deposits (Fig. 12). Partial verification of modeled runout velocities is possible at overtopped features, such as the hill at Schwarenbach, with the following (see, e.g., Evans et al., 2001; Jibson et al., 2006):

$$v_{min} = (2gh)^{0.5}$$

Because basal and internal friction are neglected in this formulation, v_{min} represents the minimum velocity needed to achieve the observed runup height h (g is gravitational acceleration). Estimated v_{min} at Schwarenbach ($h = 135$ m) is 51 m s^{-1}, consistent with our predicted model velocity of 60 m s^{-1}. Runout of the Kl. Rinderhorn rock avalanche attained a maximum simulated velocity of ~110 m s^{-1}, which is near the upper limit of comparable results in other model studies (Hungr and Evans, 1996); however, frictional basal rheology can overestimate velocities (Hungr et al., 2005).

Application of a reduced friction angle for the valley sediments at Kl. Rinderhorn may be explained by entrained material and rapid undrained loading. Entrainment of saturated sediments, snow, ice, or surface water into a rock avalanche, as well as rapid undrained loading reducing effective stresses because of increased pore pressure at the slide base, can increase mobility of the debris and lower the apparent friction coefficient (Hungr and Evans, 2004; Dufresne et al., 2010; Schneider et al., 2011). Valley fill in the Spittelmatte area could provide water-saturated sediments during runout and thus increase mobility for the Kl. Rinderhorn rock avalanche. All applied basal friction angles are within the range of typical values for rock avalanches (between 11° and 31°) determined from previous case-history back analyses (Hungr and Evans, 1996; Sosio et al., 2011). Overall, results of our simulations validate the hypothesis that both rock avalanches failed in a

Table 3
Physical parameters resulting from volume analysis of the Daubensee and Kl. Rinderhorn rock avalanches.

	Unit	Daubensee	Kl. Rinderhorn
Source volume	(10^6 m^3)	4.4	36.7
Source area	(km^2)	0.13	0.37
Mean source thickness	(m)	35	101
Rock type		Tithonian limestone	Valanginian limestone
Deposit volume	(10^6 m^3)	4.2[a]	46.6
Deposit area	(km^2)	0.58[a]	2.10
Mean deposit thickness	(m)	7	22
Bulking factor	(%)	25[b]	27
Fahrböschung angle	(°)	21	14

[a] Calculated deposit volume and area for the Daubensee rock avalanche does not include unidentified deposits in the lake.
[b] The bulking factor for the Daubensee rock avalanche is the estimated value for runout models including assumed deposits in the lake.

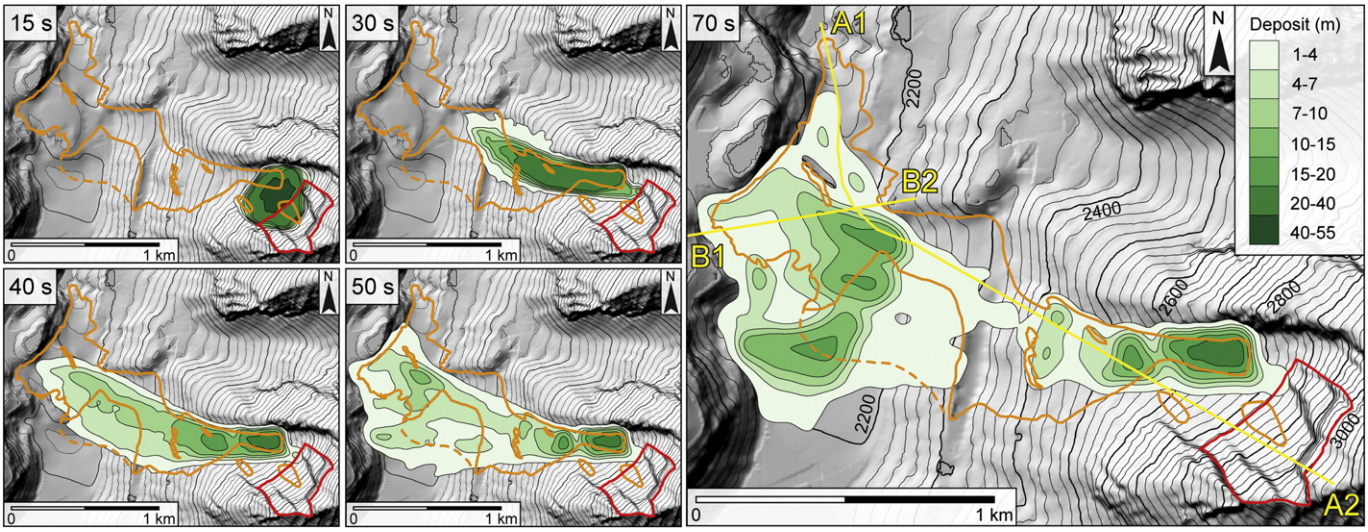

Fig. 9. Runout model for the Daubensee rock avalanche: Isopach maps of the deposit assuming frictional rheology compared to deposit outlines from field observations (orange line) at time steps of 15, 30, 40, 50, and 70 s after failure initiation. Longitudinal profile along runout path and cross sections through deposit (yellow lines) shown in Fig. 10.

catastrophic manner and that the large observed runout distances are plausible assuming typical basal friction angles; runout over glacier ice is not required in either case (as previously assumed, e.g., by Abele, 1974).

8. Preconditioning, preparatory and triggering factors

To better understand failure of the Rinderhorn rock avalanches in a paraglacial context (Ballantyne, 2002; McColl, 2012), it is important to analyze time-dependent failure mechanisms, collectively referred to as progressive failure (Terzaghi, 1962), or processes that lead to degradation of rock mass strength and ultimately slope failure (Eberhardt et al., 2004). Rock slope stability is at the fundamental level controlled by inherited structure (Terzaghi, 1962; Augustinus, 1995; Moore et al., 2009). Steep, valley-dipping sedimentary bedding, weak interlayered beds of marl, and karstification contribute to the high predisposition for dip-slope sliding on the eastern flanks in the Rinderhorn region.

Both rock slope failures investigated in this study occurred during the early Holocene, several thousand years after deglaciation of the valley flanks. With such a large lag time, deglaciation processes (e.g., glacial debuttressing) were likely not the predominant factor leading to ultimate failure. However, glacial erosion conditioned both slope failures by undercutting and exposing slopes in steeply dipping limestone, making failure kinematically feasible. Valley deepening can also lead to increased stresses on rock bridges connecting non-persistent discontinuities, reducing slope stability (Augustinus, 1995; Leith et al., 2014). Fatigue mechanisms may further contribute to time-dependent rock mass strength degradation (e.g., thermo- and hydro-mechanical stress cycles), preparing paraglacial valley slopes for failure until limit equilibrium is reached (Eberhardt et al., 2004; Prager et al., 2008; McColl, 2012).

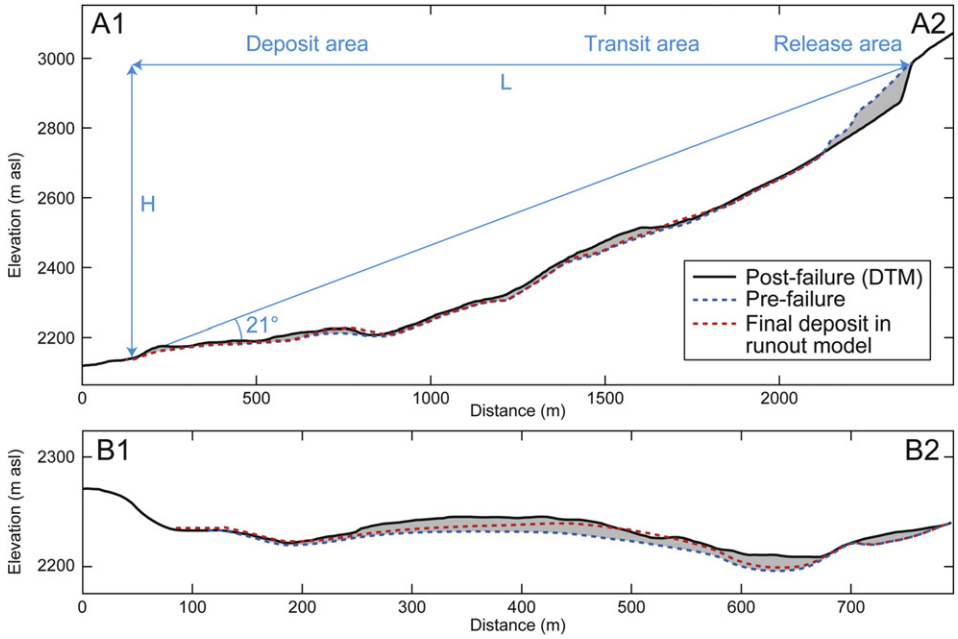

Fig. 10. Longitudinal profile along the runout path, and cross section through deposit of the Daubensee rock avalanche, showing estimated and modeled source and deposit thickness.

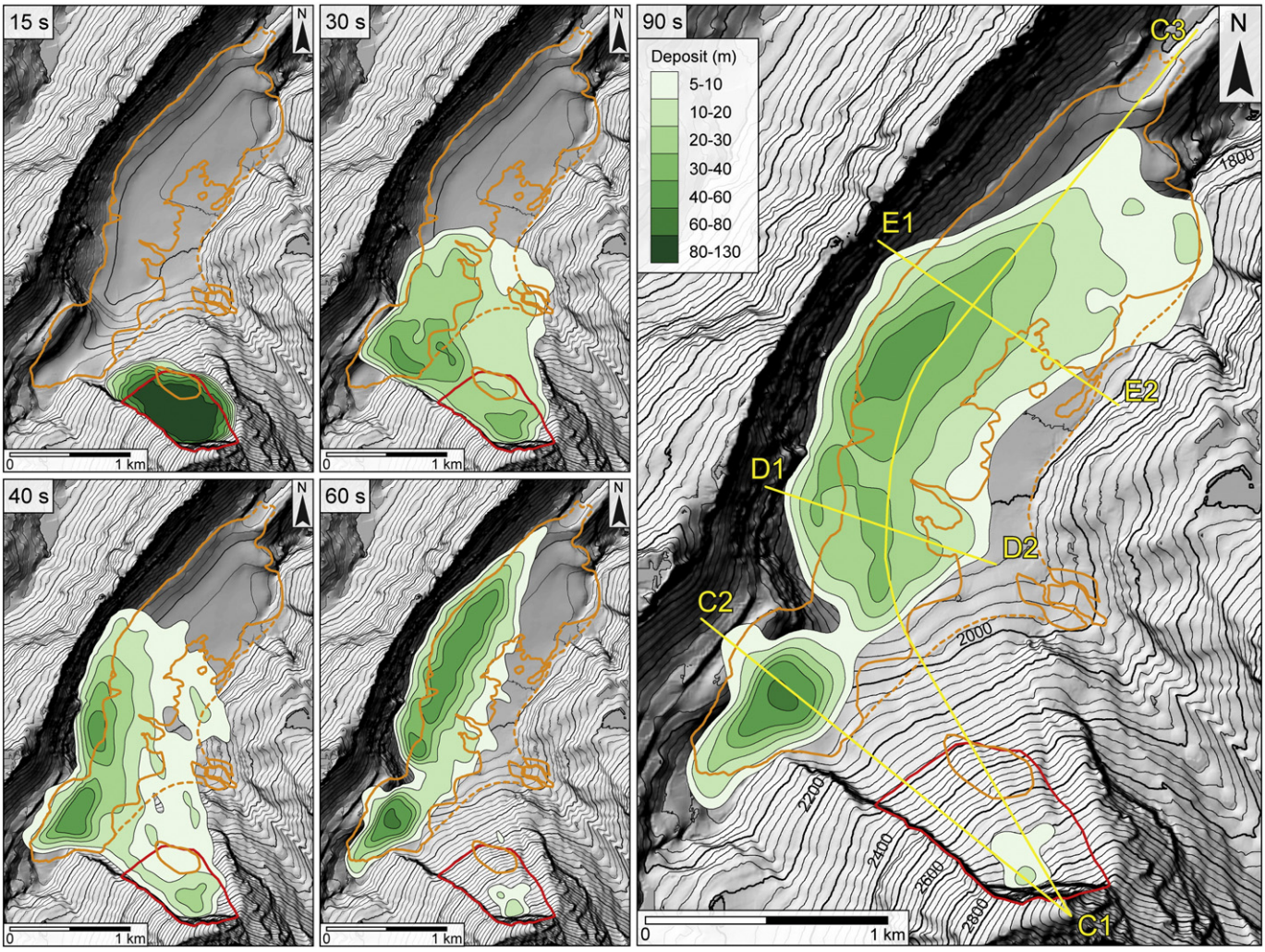

Fig. 11. Runout model for the Kl. Rinderhorn rock avalanche: Isopach maps of the deposit assuming frictional rheology compared to deposit outlines from field observations (orange line) at time steps of 15, 30, 40, 60, and 90 s after failure initiation. Longitudinal profile along runout path and cross sections through deposit (yellow lines) shown in Fig. 12.

Climate conditions during the early Holocene were cold and dry (Ivy-Ochs et al., 2006; Kerschner and Ivy-Ochs, 2008), but the Preboreal/Boreal represents a climatic transition toward a warmer and wetter environment (Haas et al., 1998; Tinner and Kaltenrieder, 2005). Holocene climate change may have influenced slope stability at the Rinderhorn. Increased temperatures can affect the strength of ice-filled discontinuities high in the release areas (Draebing et al., 2014) or melt ice promoting increased joint-water pressures (Fischer et al., 2010). In addition, more frequent heavy rainfall events coinciding with a wetter climate may affect rock slope stability through hydro-mechanical damage (Gischig et al., 2015). These processes drive progressive failure leading to a bulk reduction in resisting forces until ultimate failure is triggered. Despite the apparent increase in Alpine landslide activity coinciding with climate change during the onset of the Holocene (Prager et al., 2008; Ivy-Ochs et al., 2009a; Zerathe et al., 2014; Nicolussi et al., 2015), clear mechanical linkages between climate and slope stability for individual case studies remain speculative.

Stronger evidence exists for coseismic triggering of the Rinderhorn rock avalanches. The two rock avalanches failed at ~9.8 ka (this study), approximately coeval (within the uncertainty of the dating method) with the nearby Kander valley rock avalanche at ~9.6 ka (Tinner et al., 2005). This tight spatial and temporal correspondence suggests a seismic trigger, with an earthquake epicenter in the general area. The nearby Rhone valley in southern Switzerland has a history of earthquake-triggered rock avalanches; Fritsche et al. (2012) reported four known M~6 earthquakes over the past 500 years, each of which triggered multiple rock slope failures. Numerous examples also exist worldwide of multiple landslides (frequently spatially clustered) triggered by a single large earthquake (e.g., Jibson et al., 2006; Owen et al., 2008). Keefer (1984) highlighted that the area affected by landslides depends on the magnitude of the earthquake. An M~6 earthquake would be strong enough to trigger landslides within an epicentral distance of up to 100 km. In our study region, the Gemmi fault is an active NW-SE trending strike-slip fault, with two instances of post-glacial reactivation dated using luminescence techniques at 8.7 ± 2.0 ka and 2.4 ± 0.5 ka (Ustaszewski et al., 2007). Macroseismicity in this area of Switzerland, however, is not generally restricted to known active faults, having a typically more distributed pattern (Ustaszewski and Pfiffner, 2008).

Further evidence for a seismic trigger lies at the bottom of Swiss lakes. Subaquatic mass movement stratigraphy can be used to identify and date paleo-earthquakes (e.g., Strasser et al., 2013). Lacustrine mass movement deposits in Lake Lucerne and nearby Lake Seelisberg indicate a strong earthquake ($M \geq 6$) occurred in central Switzerland at 9.88–9.96 ka BP (Becker et al., 2005). Schnellmann et al. (2006) refers to the same event in sediments from Lake Lucerne dated at 9.87 ka BP. Their assumed epicenter is located in central Switzerland 60–80 km from the Rinderhorn region, requiring an earthquake with $M > 6$ to trigger large landslides over this distance (Keefer, 1984). The precise epicenter is unknown, however, and Becker et al. (2005) proposed that a

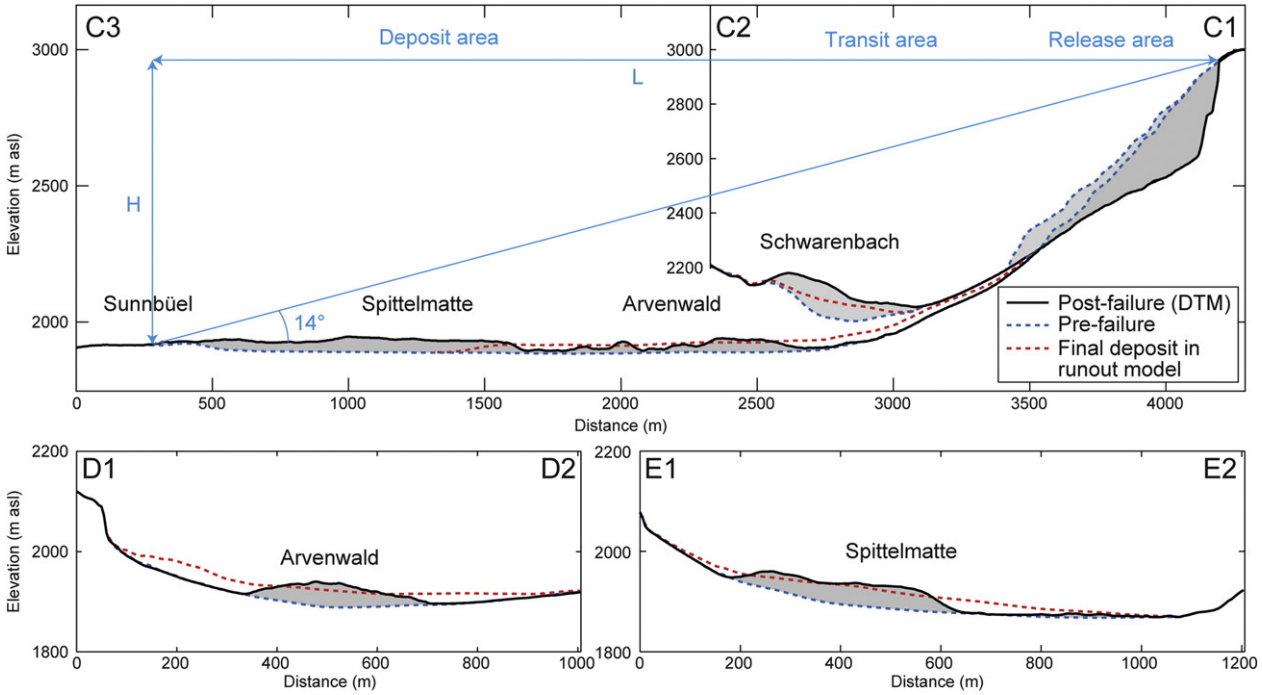

Fig. 12. Longitudinal profile along runout path, and cross sections through the deposit of the Kl. Rinderhorn rock avalanche, showing estimated and modeled source and deposit thickness.

large paleo-earthquake occurred in the central Swiss Alps at this same time. Potentially concurrent triggering of more distant landslides at Flims and in the Eastern Alps (Prager et al., 2008; Ivy-Ochs et al., 2009a; Nicolussi et al., 2015) by the same seismic event would require an earthquake with M > 7, but no evidence for a paleo-earthquake with this magnitude has been found (Strasser et al., 2006, 2013). While the origins of temporal landslide clustering at the orogen-scale remain unresolved (cf. Zerathe et al., 2014; Nicolussi et al., 2015), there is evidence for enhanced earthquake activity during the late Pleistocene/early Holocene, suggested to be caused by isostatic post-glacial rebound (Monecke et al., 2006; Strasser et al., 2013), which likely affected the entire Alps. Our results support the occurrence of a strong earthquake around ~9.8 ka, and we propose that they may help refine the estimated epicenter as nearer to the Kander valley than previously thought.

9. Conclusions

We presented detailed investigations of two rock avalanches in the Rinderhorn area of the Bernese Alps, Switzerland. Both events initiated as dip-slope sliding along sedimentary bedding, representing massive slope failure in a catastrophic manner, and developed into high-mobility rock avalanches with long runout. Key outcomes of our study are:

- The Kl. Rinderhorn rock avalanche released ~37 million m^3 of rock with a runout distance of up to 4.3 km (Fahrböschung angle = 14°). The deposit bulked to ~47 million m^3. The rock avalanche developed spatially variable deposit morphology, including a hummocky surface in the proximal region and a longitudinal flow ridge in the distal area. The distal region was later modified by fluvial erosion and by periodic ice avalanches from the neighboring Altels.
- The 4.4 million m^3 Daubensee rock avalanche had a maximum runout distance of 2.5 km (Fahrböschung angle = 21°), breaching a Lateglacial moraine and bulking to an estimated 5.5 million m^3 during deposition. Deposits are thin and spread over a large area, with several flow and push ridges. A large amount of the deposit is estimated to reside in Lake Daubensee.
- Runout behavior of the two rock avalanches was recreated in numerical simulations employing a frictional rheology. A basal friction angle of 22° was assumed for each, with a reduced value of 12° in the alluvial plain at Kl. Rinderhorn. This low basal friction angle may be related to entrained water-saturated sediments and to rapid, undrained loading along the runout path.
- Ages of the two rock avalanches constrained from ^{36}Cl surface exposure dating are coeval at 9.8 ± 0.5 ka, ruling out deglaciation as a direct trigger. The close temporal agreement of the two events, together with the contemporaneous nearby Kander valley rock avalanche as well as paleoseismic records from nearby lakes, supports the hypothesis of simultaneous earthquake triggering.

Acknowledgements

We thank Oldrich Hungr for the use of DAN3D and the Ion Beam Physics (ETH Zurich) group for ^{36}Cl and ^{14}C AMS measurements. Special thanks to Johnny Sanders for field assistance and to Christian Wirsig for help in the lab. The aerial cableway Sunnbüel AG provided transportation support. Constructive comments from A. Schomacker and two anonymous reviewers, as well as editor Richard Marston, helped improve this manuscript.

References

Aaron, J., Hungr, O., 2016. Dynamic simulation of the motion of partially-coherent landslides. Eng. Geol. 205, 1–11.
Abele, G., 1974. Bergstürze in den Alpen. Ihre Verbreitung, Morphologie und Folgeerscheinungen 25. Wissenschaftliche Alpenvereinshefte, München.
Agliardi, F., Crosta, G.B., Zanchi, A., Ravazzi, C., 2009. Onset and timing of deep-seated gravitational slope deformations in the eastern Alps, Italy. Geomorphology 103 (1), 113–129.
Alfimov, V., Ivy-Ochs, S., 2009. How well do we understand production of ^{36}Cl in limestone and dolomite? Quat. Geochronol. 4 (6), 462–474.
Alley, R.B., Meese, D.A., Shuman, C.A., Gow, A.J., Taylor, K.C., Grootes, P.M., White, J.W.C., Ram, M., Waddington, E.D., Mayewski, P.A., Zielinski, G.A., 1993. Abrupt increase in greenland snow accumulation at the end of the Younger Dryas event. Nature 362 (6420), 527–529.

Augustinus, P.C., 1995. Glacial valley cross-profile development: the influence of in situ rock stress and rock mass strength, with examples from the Southern Alps, New Zealand. Geomorphology 14 (2), 87–97.

Balco, G., 2011. Contributions and unrealized potential contributions of cosmogenic-nuclide exposure dating to glacier chronology, 1990–2010. Quat. Sci. Rev. 30 (1–2), 3–27.

Balco, G., Stone, J.O., Lifton, N.A., Dunai, T.J., 2008. A complete and easily accessible means of calculating surface exposure ages or erosion rates from ^{10}Be and ^{26}Al measurements. Quat. Geochronol. 3 (3), 174–195.

Ballantyne, C.K., 2002. Paraglacial geomorphology. Quat. Sci. Rev. 21 (18–19), 1935–2017.

Ballantyne, C.K., Wilson, P., Gheorghiu, D., Rodés, À., 2014a. Enhanced rock-slope failure following ice-sheet deglaciation: timing and causes. Earth Surf. Process. Landf. 39 (7), 900–913.

Ballantyne, C.K., Sandeman, G.F., Stone, J.O., Wilson, P., 2014b. Rock-slope failure following Late Pleistocene deglaciation on tectonically stable mountainous terrain. Quat. Sci. Rev. 86, 144–157.

Becker, A., Ferry, M., Monecke, K., Schnellmann, M., Giardini, D., 2005. Multiarchive paleoseismic record of late Pleistocene and Holocene strong earthquakes in Switzerland. Tectonophysics 400 (1–4), 153–177.

Bini, A., Buoncristiani, J.-F., Coutterand, S., Ellwanger, D., Felber, M., Florineth, D., Graf, H.R., Keller, O., Kelly, M., Schlüchter, C., Schoeneich, P., 2009. Die Schweiz während des letzteiszeitlichen Maximums (LGM). Bundesamt für Landestopografie swisstopo, Wabern.

Bronk Ramsey, C., Lee, S., 2013. Recent and planned developments of the program OxCal. Radiocarbon 55 (2–3), 720–730.

Christl, M., Vockenhuber, C., Kubik, P.W., Wacker, L., Lachner, J., Alfimov, V., Synal, H.A., 2013. The ETH Zurich AMS facilities: performance parameters and reference materials. Nucl. Instrum. Methods Phys. Res., Sect. B 294, 29–38.

Claude, A., Ivy-Ochs, S., Kober, F., Antognini, M., Salcher, B., Kubik, P., 2014. The Chironico landslide (Valle Leventina, southern Swiss Alps): age and evolution. Swiss J. Geosci. 107 (2–3), 273–291.

Cossart, E., Braucher, R., Fort, M., Bourlès, D.L., Carcaillet, J., 2008. Slope instability in relation to glacial debuttressing in alpine areas (Upper Durance catchment, southeastern France): evidence from field data and ^{10}Be cosmic ray exposure ages. Geomorphology 95 (1–2), 3–26.

Draebing, D., Krautblatter, M., Dikau, R., 2014. Interaction of thermal and mechanical processes in steep permafrost rock walls: a conceptual approach. Geomorphology 226, 226–235.

Dufresne, A., Davies, T.R., McSaveney, M.J., 2010. Influence of runout-path material on emplacement of the Round Top rock avalanche, New Zealand. Earth Surf. Process. Landf. 35 (2), 190–201.

Eberhardt, E., Stead, D., Coggan, J.S., 2004. Numerical analysis of initiation and progressive failure in natural rock slopes—the 1991 Randa rockslide. Int. J. Rock Mech. Min. Sci. 41 (1), 69–87.

Evans, S.G., Hungr, O., Clague, J.J., 2001. Dynamics of the 1984 rock avalanche and associated distal debris flow on Mount Cayley, British Columbia, Canada; implications for landslide hazard assessment on dissected volcanoes. Eng. Geol. 61 (1), 29–51.

Faillettaz, J., Sornette, D., Funk, M., 2011. Numerical modeling of a gravity-driven instability of a cold hanging glacier: reanalysis of the 1895 break-off of Altelsgletscher, Switzerland. J. Glaciol. 57 (205), 817–831.

Fischer, L., Amann, F., Moore, J.R., Huggel, C., 2010. Assessment of periglacial slope stability for the 1988 Tschierva rock avalanche (Piz Morteratsch, Switzerland). Eng. Geol. 116 (1–2), 32–43.

Fritsche, S., Fäh, D., Schwarz-Zanetti, G., 2012. Historical intensity VIII earthquakes along the Rhone valley (Valais, Switzerland): primary and secondary effects. Swiss J. Geosci. 105 (1), 1–18.

Furrer, H., Badoux, H., Huber, K., V. Tavel, H., 1956. Gemmi, Geologischer Atlas Schweiz 1: 25000, Blatt 32. Schweiz. geol. Kommission.

Geertsema, M., Chiarle, M., 2013. Mass-movement causes: glacier thinning. In: Shroder, J.F. (Ed.), Treatise on Geomorphology. Mountain and Hillslope Geomorphology. Academic Press, San Diego, pp. 217–222.

Gischig, V., Preisig, G., Eberhardt, E., 2015. Numerical investigation of seismically induced rock mass fatigue as a mechanism contributing to the progressive failure of deep-seated landslides. Rock Mech. Rock. Eng. 1–22.

Gosse, J.C., Phillips, F.M., 2001. Terrestrial in situ cosmogenic nuclides: theory and application. Quat. Sci. Rev. 20, 1475–1560.

Haas, J.N., Richoz, I., Tinner, W., Wick, L., 1998. Synchronous Holocene climatic oscillations recorded on the Swiss Plateau and at timberline in the Alps. The Holocene 8 (3), 301–309.

Hajdas, I., 2008. Radiocarbon dating and its applications in Quaternary studies. Quaternary Science Journal 57 (2), 2–24.

Hantke, R., 1980. Eiszeitalter II. Die jüngste Erdgeschichte der Schweiz und ihrer Nachbargebiete. Letzte Warmzeiten, Würm-Eiszeit, Eisabbau, Nacheiszeit der Alpen-Nordseite vom Rhein- zum Rhone-System. Ott, Thun. Band 2, p. 703.

Häuselmann, P., 2008. Surface corrosion of an Alpine karren field: recent measures at Innerbergli (Siebenhengste, Switzerland). Int. J. Speleol. 37 (2), 107–111.

Heim, A., 1896. Die Gletscherlawine an der Altels am 11. 9. 1895. Neujahresblatt der Zürcherischen Naturforschenden Gesellschaft 98, 65.

Heim, A., 1932. Bergsturz und Menschenleben, Beiblatt Vierteljahresschrift der Naturforschenden Gesellschaft Zürich Zürich p. 218.

Holm, K., Bovis, M., Jakob, M., 2004. The landslide response of alpine basins to post-Little Ice Age glacial thinning and retreat in southwestern British Columbia. Geomorphology 57 (3–4), 201–216.

Hungr, O., 1995. A model for the runout analysis of rapid flow slides, debris flows and avalanches. Can. Geotech. J. 32, 610–623.

Hungr, O., Evans, S.G., 1996. Rock avalanche runout prediction using a dynamic model. In: Senneset, K. (Ed.), Proceedings of the 7th International Symposium on Landslides, Trondheim, Norway, 17–21 June 1996. A.A. Balkema, Rotterdam, The Netherlands, pp. 233–238.

Hungr, O., Evans, S.G., 2004. Entrainment of debris in rock avalanches: an analysis of a long run-out mechanism. Geol. Soc. Am. Bull. 116 (9–10), 1240–1252.

Hungr, O., McDougall, S., 2009. Two numerical models for landslide dynamic analysis. Comput. Geosci. 35 (5), 978–992.

Hungr, O., Corominas, J., Eberhardt, E., 2005. Estimating landslide motion mechanism, travel distance and velocity. In: Hungr, O., Fell, R., Couture, R., Eberhardt, E. (Eds.), Proceedings of the International Conference on Landslide Risk Management. Vancouver Taylor and Francis Group, London, pp. 99–128.

Ivy-Ochs, S., 2015. Glacier variations in the European Alps at the end of the last glaciation. Cuadernos de Investigacion Geografica 41 (2), 295–315.

Ivy-Ochs, S., Kober, F., 2008. Surface exposure dating with cosmogenic nuclides. Quaternary Science Journal 57 (1–2), 179–209.

Ivy-Ochs, S., Heuberger, H., Kubik, P.W., Kerschner, H., Bonani, G., Frank, M., Schlüchter, C., 1998. The age of the Köfels event. Relative, ^{14}C and cosmogenic isotope dating of an early Holocene landslide in the Central Alps (Tyrol, Austria). Z. Gletscherk. Glazialgeol. 34, 57–68.

Ivy-Ochs, S., Synal, H.-A., Roth, C., Schaller, M., 2004. Initial results from isotope dilution for Cl and ^{36}Cl measurements at the PSI/ETH Zurich AMS facility. Nucl. Instrum. Methods Phys. Res., Sect. B 223–224, 623–627.

Ivy-Ochs, S., Kerschner, H., Reuther, A., Maisch, M., Sailer, R., Schaefer, J., Kubik, P.W., Synal, H.-A., Schlüchter, C., 2006. The timing of glacier advances in the northern European Alps based on surface exposure dating with cosmogenic ^{10}Be, ^{26}Al, ^{36}Cl, and ^{21}Ne. Geol. Soc. Am. Spec. Pap. 415, 43–60.

Ivy-Ochs, S., Kerschner, H., Reuther, A., Preusser, F., Heine, K., Maisch, M., Kubik, P.W., Schlüchter, C., 2008. Chronology of the last glacial cycle in the European Alps. J. Quat. Sci. 23 (6–7), 559–573.

Ivy-Ochs, S., Poschinger, A.v., Synal, H.A., Maisch, M., 2009a. Surface exposure dating of the flims landslide, Graubünden, Switzerland. Geomorphology 103 (1), 104–112.

Ivy-Ochs, S., Kerschner, H., Maisch, M., Christl, M., Kubik, P.W., Schlüchter, C., 2009b. Latest Pleistocene and Holocene glacier variations in the European Alps. Quat. Sci. Rev. 28 (21−22), 2137–2149.

Jibson, R.W., Harp, E.L., Schulz, W., Keefer, D.K., 2006. Large rock avalanches triggered by the M 7.9 Denali Fault, Alaska, earthquake of 3 November 2002. Eng. Geol. 83 (1–3), 144–160.

Keefer, D.K., 1984. Landslides caused by earthquakes. Geol. Soc. Am. Bull. 95 (4), 406–421.

Kerschner, H., Ivy-Ochs, S., 2008. Palaeoclimate from glaciers: examples from the Eastern Alps during the Alpine Lateglacial and early Holocene. Glob. Planet. Chang. 60 (1–2), 58–71.

Korup, O., 2006. Rock-slope failure and the river long profile. Geology 34 (1), 45–48.

Leith, K., Moore, J.R., Amann, F., Loew, S., 2014. Subglacial extensional fracture development and implications for Alpine valley evolution. J. Geophys. Res. Earth Surf. 119 (1), 62–81.

Martin, S., Campedel, P., Ivy-Ochs, S., Viganò, A., Alfimov, V., Vockenhuber, C., Andreotti, E., Carugati, G., Pasqual, D., Rigo, M., 2014. Lavini di Marco (Trentino, Italy): ^{36}Cl exposure dating of a polyphase rock avalanche. Quat. Geochronol. 19, 106–116.

McColl, S.T., 2012. Paraglacial rock-slope stability. Geomorphology 153–154, 1–16.

McColl, S.T., Davies, T.R.H., 2013. Large ice-contact slope movements: glacial buttressing, deformation and erosion. Earth Surf. Process. Landf. 38 (10), 1102–1115.

McColl, S.T., Davies, T.R.H., McSaveney, M.J., 2010. Glacier retreat and rock-slope stability: debunking debuttressing. Delegate papers, geologically active. 11th Congress of the International Association for Engineering Geology and the Environment, Auckland, Aotearoa. 5–10, pp. 467–474 September 2010. (Auckland, New Zealand).

McDougall, S., Hungr, O., 2004. A model for the analysis of rapid landslide motion across three-dimensional terrain. Can. Geotech. J. 41 (6), 1084–1097.

Monecke, K., Anselmetti, F., Becker, A., Schnellmann, M., Sturm, M., Giardini, D., 2006. Earthquake-induced deformation structures in lake deposits: a late Pleistocene to Holocene paleoseismic record for Central Switzerland. Eclogae Geol. Helv. 99 (3), 343–362.

Moore, J.R., Sanders, J.W., Dietrich, W.E., Glaser, S.D., 2009. Influence of rock mass strength on the erosion rate of alpine cliffs. Earth Surf. Process. Landf. 34 (10), 1339–1352.

Nagelisen, J., Moore, J.R., Vockenhuber, C., Ivy-Ochs, S., 2015. Post-glacial rock avalanches in the Obersee valley, Glarner alps, Switzerland. Geomorphology 238, 94–111.

Nicolussi, K., Spötl, C., Thurner, A., Reimer, P.J., 2015. Precise radiocarbon dating of the giant Köfels landslide (Eastern Alps, Austria). Geomorphology 243, 87–91.

Ostermann, M., Sanders, D., Ivy-Ochs, S., Alfimov, V., Rockenschaub, M., Römer, A., 2012. Early Holocene (8.6 ka) rock avalanche deposits, Obernberg valley (Eastern Alps): landform interpretation and kinematics of rapid mass movement. Geomorphology 171–172, 83–93.

Owen, L.A., Kamp, U., Khattak, G.A., Harp, E.L., Keefer, D.K., Bauer, M.A., 2008. Landslides triggered by the 8 October 2005 Kashmir earthquake. Geomorphology 94 (1–2), 1–9.

Patzelt, G., 2012. Die Bergstürze vom Tschirgant und von Haiming, Oberinntal, Tirol. Begleitworte zur Kartenbeilage. Jahrbuch der Geologischen Bundesanstalt 152 (1–4), 13–24.

Prager, C., Zangerl, C., Patzelt, G., Brandner, R., 2008. Age distribution of fossil landslides in the Tyrol (Austria) and its surrounding areas. Nat. Hazards Earth Syst. Sci. 8 (2), 377–407.

Prager, C., Ivy-Ochs, S., Ostermann, M., Synal, H.A., Patzelt, G., 2009. Geology and radiometric ^{14}C-, ^{36}Cl- and Th-/U-dating of the Fernpass rockslide (Tyrol, Austria). Geomorphology 103 (1), 93–103.

Reimer, P.J., Bard, E., Bayliss, A., Beck, J.W., Blackwell, P.G., Bronk Ramsey, C., Buck, C.E., Cheng, H., Edwards, R.L., Friedrich, M., Grootes, P.M., Guilderson, T.P., Haflidason, H., Hajdas, I., Hatté, C., Heaton, T.J., Hoffmann, D.L., Hogg, A.G., Hughen, K.A., Kaiser, K.F., Kromer, B., Manning, S.W., Niu, M., Reimer, R.W., Richards, D.A., Scott, E.M., Southon, J.R., Staff, R.A., Turney, C.S.M., van der Plicht, J., 2013. IntCal13 and marine13

radiocarbon age calibration curves 0–50,000 years cal BP. Radiocarbon 55 (4), 1869–1887.
Robinson, T., Davies, T.H., Reznichenko, N., De Pascale, G., 2014. The extremely long-runout Komansu rock avalanche in the Trans Alai range, Pamir Mountains, southern Kyrgyzstan. Landslides 1–13.
Schneider, D., Huggel, C., Haeberli, W., Kaitna, R., 2011. Unraveling driving factors for large rock–ice avalanche mobility. Earth Surf. Process. Landf. 36 (14), 1948–1966.
Schnellmann, M., Anselmetti, F., Giardini, D., McKenzie, J., 2006. 15,000 years of mass-movement history in Lake Lucerne: implications for seismic and tsunami hazards. Eclogae Geol. Helv. 99 (3), 409–428.
Sharma, P., Kubik, P.W., Fehn, U., Gove, H.E., Nishiizumi, K., Elmore, D., 1990. Development of ^{36}Cl standards for AMS. Nucl. Instrum. Methods Phys. Res., Sect. B 52 (3), 410–415.
Soldati, M., Corsini, A., Pasuto, A., 2004. Landslides and climate change in the Italian Dolomites since the Late glacial. Catena 55 (2), 141–161.
Sosio, R., Crosta, G., Hungr, O., 2011. Numerical modeling of debris avalanche propagation from collapse of volcanic edifices. Landslides 1–20.
Stone, J.O., Allan, G.L., Fifield, L.K., Cresswell, R.G., 1996. Cosmogenic chlorine-36 from calcium spallation. Geochim. Cosmochim. Acta 60 (4), 679–692.
Stone, J.O.H., Evans, J.M., Fifield, L.K., Allan, G.L., Cresswell, R.G., 1998. Cosmogenic chlorine-36 production in calcite by muons. Geochim. Cosmochim. Acta 62 (3), 433–454.
Strasser, M., Anselmetti, F.S., Fäh, D., Giardini, D., Schnellmann, M., 2006. Magnitudes and source areas of large prehistoric northern Alpine earthquakes revealed by slope failures in lakes. Geology 34 (12), 1005–1008.
Strasser, M., Monecke, K., Schnellmann, M., Anselmetti, F.S., 2013. Lake sediments as natural seismographs: a compiled record of Late Quaternary earthquakes in Central Switzerland and its implication for Alpine deformation. Sedimentology 60 (1), 319–341.
Terzaghi, K., 1962. Stability of steep slopes on hard unweathered rock. Géotechnique 12 (4), 251–270.
Tinner, W., Kaltenrieder, P., 2005. Rapid responses of high-mountain vegetation to early Holocene environmental changes in the Swiss Alps. J. Ecol. 93 (5), 936–947.
Tinner, W., Kaltenrieder, P., Soom, M., Zwahlen, P., Schmidhalter, M., Boschetti, A., Schlüchter, C., 2005. Der nacheiszeitliche Bergsturz im Kandertal (Schweiz): alter und Auswirkungen auf die damalige umwelt. Eclogae Geol. Helv. 98, 83–95.
Ustaszewski, M., Pfiffner, O.A., 2008. Neotectonic faulting, uplift and seismicity in the central and western Swiss Alps. Geol. Soc. Lond., Spec. Publ. 298 (1), 231–249.
Ustaszewski, M., Herwegh, M., McClymont, A.F., Pfiffner, O.A., Pickering, R., Preusser, F., 2007. Unravelling the evolution of an Alpine to post-glacially active fault in the Swiss Alps. J. Struct. Geol. 29 (12), 1943–1959.
Van Husen, D., Ivy-Ochs, S., Alfimov, V., 2007. Mechanism and age of late glacial landslides in the Calcareous Alps; the Almtal, Upper Austria. Aust. J. Earth Sci. 100, 114–126.
Wacker, L., Bonani, G., Friedrich, M., Hajdas, I., Kromer, B., Nemec, N., Ruff, M., Suter, M., Synal, H.-A., Vockenhuber, C., 2010. In: MICADAS (Ed.), Routine and High-Precision Radiocarbon Dating (2010).
Zerathe, S., Lebourg, T., Braucher, R., Bourlès, D., 2014. Mid-Holocene cluster of large-scale landslides revealed in the Southwestern Alps by ^{36}Cl dating. Insight on an Alpine-scale landslide activity. Quat. Sci. Rev. 90, 106–127.